Elastic Slowing of Supersonic Beams with an Atomic Mirror

by

Christoph Jan Schaeff

THESIS

Presented to the Faculty of the Graduate School of
The University of Texas at Austin
in Partial Fulfillment
of the Requirements
for the Degree of

MASTER OF ARTS

THE UNIVERSITY OF TEXAS AT AUSTIN
December 2008

Elastic Slowing of Supersonic Beams with an Atomic Mirror

APPROVED BY

SUPERVISING COMMITTEE:

Mark G. Raizen, Supervisor

George T. Shubeita

Acknowledgments

This work would not have been possible without the help and support I received during my stay in Austin. It is a pleasure for me to thank those people.

Foremost, I would like to thank my supervisor Prof. Mark Raizen, his friendliness and helpfulness make working in the group so enjoyable and constructive. I am honored that I was given the opportunity to work in this group. Thank a lot for all the help and support!

I wish to express my thank to Ed Narevicius, our former post-doc, for all his constructive comments and help.

Many thanks to the slow beam group: Adam Libson, for his patience, detailed explanations and help during the year, Isaac Chavez, who was always there to help me out and to answer crucial questions about football rules, Tom Mazur, Julia Majors and Christian Parthey. I learned a lot from all of you, thanks!

Many thanks to the whole rest of the group: Charlotte Sanders, David Medellin, Gabriel Price, Hrishikesh Kelkar, Kirsten Viering, Travis Bannerman, and Tongcang Li. You all contributed to the great working environment and atmosphere. I had a great time working with all of you guys!

I am indebted to the whole machine shop, especially to Allen and Jack for their always friendly and helpful advices, as well as to Georg and the rest for the great job on building my parts.

I owe my gratitude to Dr. Bill Lackowsky and Mike Tiner from the Center for Nano & Molecular Science & Technology for all of their instructions, help and troubleshooting on all of the various equipment I got to use during my stay.

I am grateful to Olga Vera, Elena Simmons, Vanessa Munoz and Becky Valdez for assisting me in many different ways and keeping the department organized.

I like to thank Dr. Donald MacLaren from the University of Glasgow for very helpful discussions and advices on lithium fluoride.

I also wish to thank Prof. George Shubeita for agreeing to be on my supervising committee.

I gratefully acknowledge Prof. Fink, Prof. Assaad and Prof. Langhoff, the University of Texas at Austin and the Julius-Maximilians Universitaet Wuerzburg for letting me participate in this great exchange program.

I am indebted to the DAAD for its generous financial support.

Thanks to all my former roomates: Christian, Ruben, Johannes, Julia and Andrea for a funny time exploring the American culture.

I owe my loving thanks to Friederike. Without her understanding and patience over the last year, it would have been impossible for me to finish this work.

My deepest gratitude goes to my family for all their support throughout my whole life...

...and my warmest thanks to everyone I have failed to mention, every new friend, old friend and every person I met in or outside the RLM and who made my stay in Austin so pleasant and wonderful.
I had a great time!

- Christoph

The University of Texas at Austin, December 2008

Elastic Slowing of Supersonic Beams with an Atomic Mirror

Christoph Jan Schaeff, M.A.
The University of Texas at Austin, 2008

Supervisor: Mark G. Raizen

In this thesis a method of slowing supersonic beams of neutral atoms by elastic reflection from a receding mirror, mounted on the tip of a spinning rotor, is presented, advances and improvements are described. Special attention is brought to the atomic mirror, since the efficiency of the experiment critically depends on its reflectivity. The use of hydrogen passivated silicon(111) as a mirror is examined. The short lifetime and complicated preparation lead to the use of a different material. By cleaving a radiation hardened lithium fluoride single crystal along the (100) plane we succeeded in finding a very inert and easy to prepare atomic mirror. First results of helium elastically scattered from a static and moving mirror of lithium fluoride are presented.

Table of Contents

Chapter 1

Introduction

Since the 1970s growing attention has been shifted towards controlling atomic motion. Since then a number of Nobel Prizes have been awarded to people working in that area [1] reflecting the growing interest and importance of this field. New techniques have opened several opportunities for new science, such as the study of fundamental physical phenomena and precision measurement. Besides new methods of cooling and trapping, techniques for manipulating atomic beams were developed. The de Broglie wavelength $\lambda \propto 1/v$ of atoms at low velocity v now can be on the order of atomic bonds and lattice constants leading to a whole new field called Atom Optics. Besides light forces as a tool for controlling atomic motion, atom mirrors, lenses [2] [3], gratings, and beam splitter were developed. These new tools made it possible to build an atomic interferometer [4] and even microscopes using helium atoms are developed [5].

All of these techniques require a beam of cold atoms or molecules. Unfortunately, the common methods used today for obtaining cold atoms rely on certain atomic properties. Laser cooling for example requires a certain atomic energy structure while evaporative cooling requires a non-zero magnetic moment. If the atom or molecule does not meet these requirements, it cannot be cooled using these techniques. Therefore only a small fraction of the periodic table is accessible using today's cooling methods.

In the Raizen Lab different approaches have been developed towards a more general cooling method. An 'atomic coilgun' has been developed using pulsed magnetic fields feasible for every atom or molecule with a magnetic moment [6]. A great fraction of the periodic table is either paramagnetic or can be excited to a metastable state with a nonzero magnetic moment making the coilgun a general method. However, if one wants to cool atoms with zero magnetic moment (for example molecular hydrogen H_2), or ground state atoms (such as ground state noble gases) neither the atomic coilgun nor common cooling methods can be used. Those atoms and molecules are of great theoretical and experimental interest (also due to their inertness).

One new approach also developed in the Raizen Lab is the slowing of atoms and molecules by reflection from a receding mirror. This mechanical approach does not depend on any internal properties of the particles such as magnetic moment, polarizability or energy state structure. Its efficiency only depends on the particle's mass and reflectivity from a surface. This approach has already been demonstrated. As reported in [7] and [8] a beam of Helium atoms at $511m/s$ was successfully slowed to $246m/s$ with a temperature of $250mK$ in the co-moving frame with this experiment. Advances in this experiment will be described in this thesis.

In **chapter 2** an overview of the experiment will be given and important parts of the setup will be discussed. Chapter 3 and 4 will deal with the challenge of creating atomically flat surfaces aiming towards higher reflectivity.

Chapter 3 will consider the creation of atomic mirrors from silicon wafers. Those wafers are etched by an irreversible chemical process resulting in an atomically flat surface. They are passivated with hydrogen to improve the crystal lifetime. First the basic mechanisms behind etching and passivation of silicon will be explained followed by the experimental realization. Although the functioning of this method has already been shown [7], it faces some difficult experimental problems. Those problems lead to the use of a different material for atomic mirrors described in the following chapter.

Chapter 4 describes the use of lithium fluoride single crystals as atomic mirrors. First the process of cleaving a crystal will be explained by giving a short introduction into the theory of the dynamics of cracks. With that knowledge conclusions for the cleavage apparatus will be drawn and its design will be explained.

Chapter 5 will give a summary of improvements and changes made on the rotor experiment besides the atomic mirrors.

Eventually in **chapter 6** results will be presented followed by a short summary and perspective on possible future work in **chapter 7**.

Chapter 2

The Rotor Apparatus

2.1 Principle of Operation

In order to slow neutral atoms, not accessible to laser cooling without a zero electric or magnetic moment, one has to find a different way. One way is the mechanic approach realized in this experiment. A particle elastically reflected by a receding mirror has a lower kinetic energy expressed by the following formula:

$$v' = -v + 2v_m, \tag{2.1}$$

where v is the inital, v' the final and v_m the mirror velocity. The same also holds true for atoms, and one can therefore cool or slow a beam of atoms or molecules independent of their electro-magnetic properties or energy levels. The way this method can be realized is described in the following sections of this chapter.

2.2 Experimental Overview

In this section an overview of the rotor experiment will be given. In the following sections the basic working principle for important parts of the experiment will be explained briefly. A schematic sketch of the setup is shown

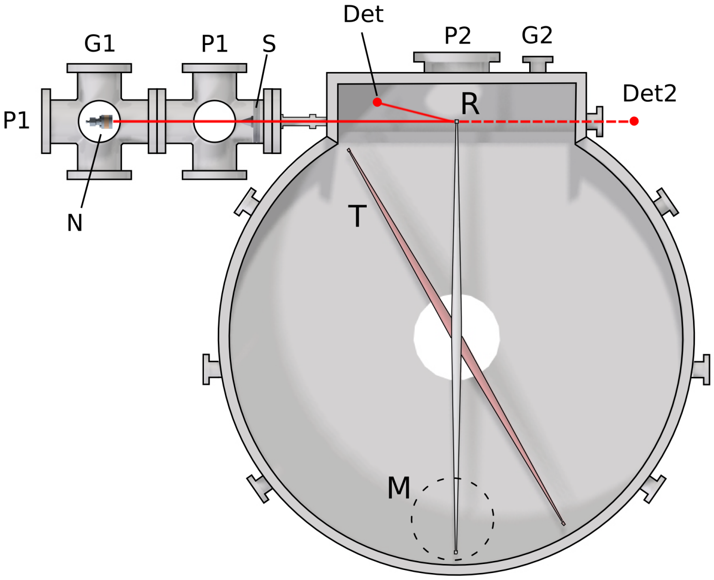

Figure 2.1: Schematic overview of the experiment. N: Nozzle, S: Skimmer, R: reflecting position, T: trigger position, Det: detector positions, P: turbo-pumps, G: vacuum gages, M: cryo-finger and crystal mount.

in Fig.2.1. The apparatus is divided in two parts. In the nozzle chamber, consisting of two 6-way crosses, an atomic beam is created and prepared. In the main chamber the beam is manipulated and detected.

Starting at the beginning, a pulsed supersonic nozzle is used as an atomic beam source (S in Fig.2.1). As it will be discussed in section 2.4 in more detail, very sharp, short, high intensity pulses of atoms can be created. Following the path of the atoms, the beam (solid red line) passes a skimmer (S in Fig.2.1) and reaches the main chamber. If the rotor is in the reflecting position (R), the beam hits the mirror mounted on the tip on each sides of the rotor. Hitting the mirror a fraction of the atoms undergoes elastic reflection (see Chap.2.5).

The rotor can also be moved in a different position such that the beam passes the main chamber and the direct beam (dashed red line) can be observed. In case of a spinning rotor, the nozzle and rotor are synchronized in such a way that the rotor passes the triggering point (T) exactly when the nozzle pulses. The atoms will then, always hit the spinning rotor at the right position. The fraction of atoms being reflected from the receding mirror show a decrease in velocity after reflection (see Eq.2.1). The beam temperature is therefore decreased (Sec.2.5).

The reflection probability of atoms from this mirror is critical for the experiment. Therefore, creating such highly reflective atomic mirrors with a long life-time is one main part of this thesis (Sec.2.5). Both, the reflected and specular beam are detected by two detectors, Det1 and Det2 in Fig.2.1, as described in Sec.2.7.

2.3 Vacuum System

The skimmer (S in Fig.2.1) has an diameter of Ø5 mm and cuts off a great fraction of the beam keeping unwanted noise, such as back scattered shock waves, out of the main chamber. The conductance of the skimmer due to the small diameter is also very low between the two chambers. This allows us to use two separated pumping systems. The main chamber pressure can be kept at about an order of magnitude lower than in the nozzle chamber. Two 360 l/min at P1 and one 600 l/min turbo-molecular pumps at P2 are used as well as two separate vacuum pressure gages at G1 and G2. Also, to further improve vacuum, a cold trap has been designed and is mounted on M in Fig.2.1. This allows faster pumping down as well as reaching much lower pressure which is an important point in terms of mirror lifetime (see Sec.2.5). After an overnight bake-out and use of the cold trap a pressure on the order of 10^{-10} *torr* can be reached with a closed nozzle.

2.4 Molecular Beams

In order to obtain atom source with high brightness, a nozzle producing pulses of supersonic atoms or molecules is used. Supersonic beams have some important advantages over other techniques such as thermal beams. In order to understand those properties the principles of operation of supersonic beams and their source is explained.

In general, atomic beams are created by letting gas in a reservoir escape through an aperture into a vacuum. In a regime where the mean free path of the gas particles is much larger than the system's aperture size one gets an effusive beam with the well-known Maxwell velocity distribution:

$$f_{(v)} = \frac{4}{\sqrt{\pi}} \left(\frac{m}{2kT}\right)^{\frac{3}{2}} \; v^2 e^{-2mv^2/2kT}.$$

Here v is the final velocity of the gas, m the particle mass, k the Boltzmann constant and T the temperature. The most probable velocity v_p and the velocity spread σ_v are given by:

$$v_p = \sqrt{\frac{2kT}{m}} \text{ and } \sigma_v = \sqrt{\frac{kT}{m}} \quad \Rightarrow \frac{\sigma_v}{v_p} = \frac{1}{\sqrt{2}}. \tag{2.2}$$

As seen in Eq.2.2 an effusive beam has quite a broad spread on the order of 70% of v_P.

However, the mean free path Λ changes with temperature T, pressure p and density ρ: $\Lambda \propto T/(p \cdot \rho)$. Therefore the pressure of the reservoir can be increased to a point where the mean free path is comparable to the aperture size and collisions between particles have to be taken into account. To describe flow properties in this regime one can use the three conservation equations: conservation of momentum ($\rho\vec{v} = 0$), conservation of mass ($\rho\frac{d\vec{v}}{dt} = -gradP$) and conservation of energy. Using those equations as well as the equation of state of an ideal gas, one can derive the following simple formula describing the change in flow velocity w, of a gass flowing through a cross-sectional area A as described in [8]:

$$\frac{dA}{A} + \frac{dw}{w}(1 - M^2) = 0. \tag{2.3}$$

Here the Mach-number $M = \frac{v}{c}$ is used which is the ratio of flow speed and sonic speed in the current medium. As seen from Eq.2.3 the flow speed of a subsonic gas ($M < 1 \Leftrightarrow v < c$) is inversely proportional to the cross-sectional area A. In the case of a supersonic gas ($M > 1$) the exact opposite relation holds.

Because of the pressure difference ΔP between reservoir and vacuum, the gas is accelerated towards the nozzle exit while the decreasing cross-section accelerates it further (see Eq.2.3 and Fig.2.2). If the pressure ratio has a certain

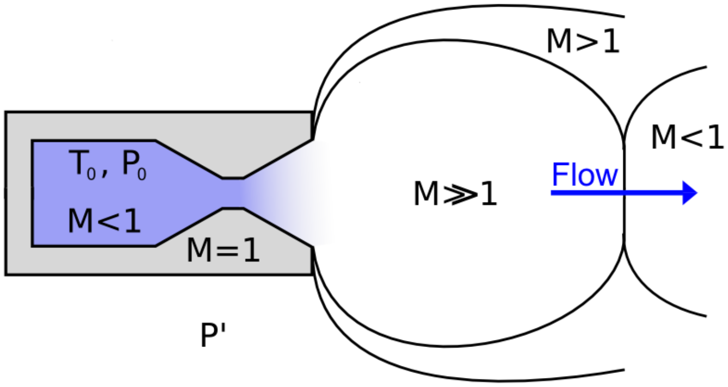

Figure 2.2: Schematic sketch of a free jet expansion into vacuum through a super-sonic nozzle.

value

$$\frac{P}{P_0} \leq \left(\frac{2}{\kappa+1}\right)^{\kappa/(\kappa-1)} \tag{2.4}$$

the gas reaches sonic speed ($M = 1$) at the exit, where $\kappa = \frac{c_P}{c_V}$ is the specific heat ratio [9]. At that point it is accelerated again, due to the decreasing cross-section area (Eq.2.3 with $M > 1$) and expands into vacuum. Therefore, in order to reach supersonic velocities a convergent-divergent nozzle is required. This principle was first used by De Laval and is thus called a Laval Nozzle as used in our experiment.

In a media information can only travel at the speed of sound. Thus, the flow of the supersonic beam does not adapt to boundary conditions it experiences in the front. Therefore, the beam can even over expand below the surrounding pressure. This causes different effects such as shock waves or the Mach disk shock. As long as the flow properties change over a distance larger than the mean-free-path, the local equilibrium is always reached instantly and the expansion can be described fully by the theory of continuous media and equilibrium thermodynamics. However, as the free beam expands into the vacuum the density decreases rapidly. When the mean free path becomes large compared to the system dimensions those theories no longer hold. The transition from a continuous flow to a non-equilibrium free molecular flow has occurred. The theoretical treatment is rather difficult and therefore only important properties of the final beam will be given. A complete derivation can be found in [9].

The final beam velocity v_f is given by

$$v_f^2 = 2\frac{\kappa}{\kappa-1}\frac{RT_0}{\bar{m}}\left[1-(\frac{P}{P_0})\right]^{\kappa/(\kappa-1)}, \tag{2.5}$$

where $\kappa = c_P/c_V$ is the specific heat ratio. This equation is also known as the St.Venant and Wantzel Equation dating back to 1839. The final beam temperature is given by

$$T = \frac{T_0}{1+\frac{\kappa}{\kappa-1}S^2}, \tag{2.6}$$

where S is the ratio between the flow speed w and most probable speed v_m. With increasing value of S the velocity distribution can be approximated by a Gauss distribution where the relative half-width Δv is given by

$$\frac{\Delta v}{w} = \frac{\Delta t}{t} = \frac{2\sqrt{2\cdot ln(2)}}{S}. \tag{2.7}$$

Here the velocity was replaced by the time of flight $\frac{\Delta v}{w} = \frac{\Delta t}{t}$ for experimental purposes.

Since the experiment aims towards cooling supersonic beams, Eq.2.5 shows two possibilities of how one can pre-cool the beam before manipulating it with the rotor. One way is to cool the nozzle gas reservoir which results in a lower final velocity. This is done in the experiment by cooling the nozzle to liquid nitrogen temperatures. Another way to pre-cool is to seed the gas with a heavier carrier gas. As already indicated in Eq.2.5 a gas mixture can be described by the average mass $\bar{m}$. Thus, by choosing a heavy carrier gas the final velocity is reduced. Unfortunately, the heavier gases tends to form energetically more favorable clusters, when in the supersonic flow region, heating the beam again. In this experiment neon (Ne, $20u$) is used.

The nozzle used in this experiment was built by Prof. Uzi Even at the Tel Aviv University. Its unique feature is its opening mechanism which creates very short pulses of atoms. $10\mu s$ FWHM pulses with a repetition rate of up to 40Hz can be achieved. The maximum backing pressure is 100atm resulting in a high intensity, monochromatic ($< 1\%$ velocity spread) and directional (7°half-angle) beam. The flux Φ from the nozzle is given by $\Phi = \frac{\rho\bar{v}}{4m}$ where $\bar{v}$ is the mean velocity. In this experiment, the nozzle is typically operated at 77K (LN_2), 4 atm and at a repetition rate of 5Hz resulting in a flux of $\Phi = 6 \cdot 10^{28}\ atoms/s/m^2$ equal to $7.5 \cdot 10^{16}$atoms/shot.

2.5 Atomic Mirror

2.5.1 Atom Surface Interaction

For this experiment a high elastic reflectivity of atoms from the surface is required. Therefor the basic interaction mechanism between incoming atoms and the surface will now be explained.

In one dimension the interaction between atoms and a surface can be described with a potential containing two additive parts: a long-range attractive force, mainly contributed by Van-der-Waals interaction, and a repulsive force due to Pauli exclusion. This leads to a characteristic potential with a minimum at z_0 and potential depth D as shown in Fig.2.3a. In addition, in two dimensions the potential has to be modulated with a corrugation function ξ to account for surface corrugations (Fig.2.3b).

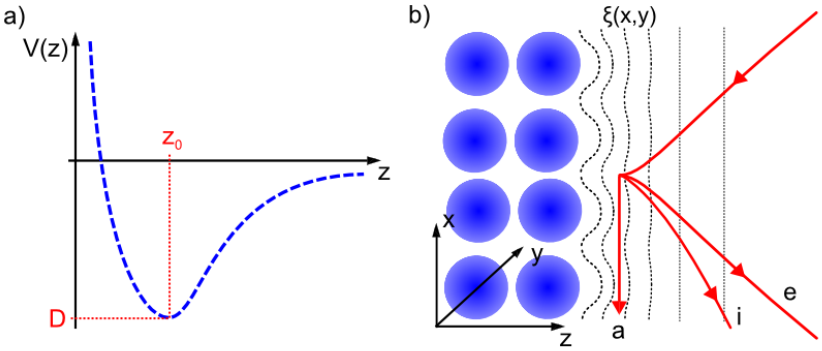

Figure 2.3: Atom- surface Interaction
(a): one-dimensional interaction potential $V(z)$, potential minimum at z_0, potential depth D. **(b)**: Interaction potential modulated with the corrugation function $\xi(x, y)$ (dashed black line). Atoms trajectories (solid red line) for different cases (i: inelastic reflection, e: elastic reflection, a: adsorption).

In general, an incident atom is diffracted if the following conditions hold [10]:

$$\Delta K = G_{nm} + \delta \quad \text{and} \quad \Delta E = \Delta.$$

Here, ΔK is the change in the incoming particle's wave vector in the surface plane, G_{nm} the number of allowed diffraction channels and ΔE the total change in kinetic energy. δ and Δ are constants representing changes in internal states of the incoming particle and the surface. As shown in (Fig.2.3b) there are four different phenomena that can occur during interaction:

- **Elastic diffraction**: $\Delta K = G_{nm}$, $\Delta E = 0$

  The particle is reflected elastically (path e in Fig.2.3b). Depending on the number of opened diffraction channels (G_{nm}) the intensity of specular reflected atoms varies.

- **Rotation inelastic diffraction**: $\Delta K = G_{nm}$, $\Delta E = \Delta E_{Rot}$

  If the incoming particle is a molecule there is the possibility of a change in the particles rotational- vibrational state $\Delta E = \Delta E_{Rot}$ (path i in Fig.2.3b). For atoms and molecules with a small rotational constant or atoms this effect is not significant.

- **Phonon inelastic diffraction**: $\Delta K = Q$, $\Delta E = G_{nm} \pm \hbar\omega$

  The particle excites or absorbs a lattice phonon with wave vector Q loosing or gaining kinetic energy equal to ΔE_{Rot} (path i in Fig.2.3b). The number of excited/absorbed phonons per atom can be estimated by the so-called Debye-Waller factor explained in Section 2.5.2.

- **Adsorption**

  In some cases, if the atom transfers enough energy to lattice phonons it can become trapped in the potential well called adsorption (path a in Fig.2.3b). In this experiment adsorption can be neglected since the incident velocity is far too high.

Taking into account the different interaction effects, only a few percent of the incoming atoms are actually reflected elastically. This number is even further reduced by temperature effects and surface perturbations described in the next two sections.

2.5.2 Inelastic and Elastic Reflections: Debye-Waller Factor

Considering a lattice at temperature $T > 0$ the atoms oscillate around their equilibrium position $r(t) = r_0 + \delta r(t)$. Because the oscillation period is small compared to the atom-surface interaction time the atom only sees the time averaged atom position $< r(t) >_t$ and the elastic scattering intensity decreases:

$$< I >_t = I_0 < e^{-i\Delta r \Delta k} >_t = I_0 e^{2W} \quad , \quad W = 12m\frac{(E_s + D)T}{\bar{M} k_B \Theta_D^2}. \tag{2.8}$$

W is called the Debye-Waller-Factor where m is the mass of the incoming atoms, $\bar{M}$ is the average mass of a surface atoms, E_s is the kinetic energy perpendicular to the surface for the incoming atom and Θ_D^2 is the crystal **surface** Debye-Temperature. The surface Debye-temperature differs from the bulk Debye-temperature. This difference comes from different force constants acting on surface atoms compared to the bulk. The approaching atoms are accelerated towards the surface changing their kinetic energy. To account for that effect, a small term D can be added to Eq.2.8 called the Beeby correction. In this simple model Θ_D^2 is a material constant. In reality it depends on the incident angle, incoming particle mass and temperature.

W describes the probability that the phonon occupation number of the crystal lattice does not change during interaction. Therefore, for a high elastic scattering intensity the crystal temperature (T) has to be small compared to Θ_D^2. This means that the chance of lattice excitations is small and therefore phonon inelastic diffraction (see Section 2.5.1) becomes small.

For a room temperature molecular helium beam ($v \approx 1870 m/s$) incident on a LiF(100) surface at 45° the reflectivity becomes about $\frac{<I>_t}{I_0} \approx 60\%$. Here a perfectly flat surface is assumed, which of course is not true (see 2.5.3). Furthermore, the specular reflectivity is reduced by the number of diffraction channels: the crystal (surface) momentum is about 1.57 1/Å while the helium atoms have a wave vector of 11.7 1/Å. The total specular reflectivity is therefore only expected to be on the order of a few percent.

2.5.3 Surface defects

Besides phonon excitations other effects, such as lattice defects, perturb the corrugation amplitude ξ on an otherwise perfectly flat surface. Examples of such defects are surface steps, lattice vacancies, adsorbed atoms, contaminations or surface oxidation. This causes a decrease in the elastic scattering intensity. Since the change in corrugation amplitude is much larger than the dimension of the defect (Fig.2.4) the scattering signal is very sensitive to the defect density.

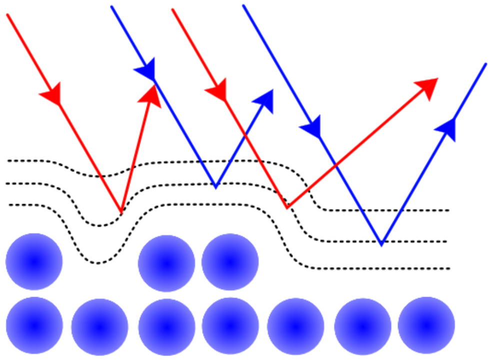

Figure 2.4: Scattering from a surface with high defect density. The perturbation of the corrugation amplitude is much bigger than the actual dislocation size leading to a high sensitivity of the elastic reflection amplitude to the defect density.

2.6 Mirror Holder

The crystal (C) in Fig.2.5 is clamped in the holder (H) by a screw (S) from the back. The thickness of the crystal can be between 1mm and about 2.5 mm. The screw has a threaded hole in it's center for tightening the hole part to the rotor tip.

2.7 Detection

The atoms are detected by a Residual Gas Analyzer (RGA). The atoms entering the ionization region of the analyzer are ionized by electron bombard-

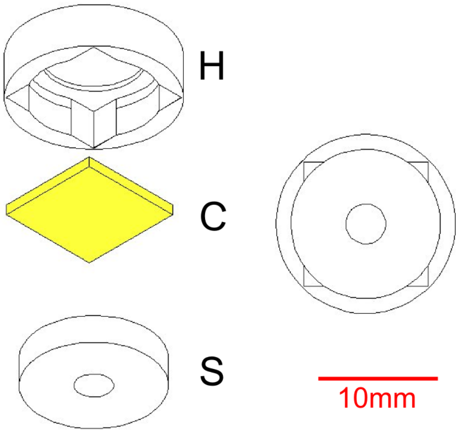

Figure 2.5: Sketch of the crystal holder. (C): crystal, (H): holder, (S): Screw.

ment from a filament. The ions are then accelerated by a biased focusing ring towards a quadrupole. This filters only atoms of a certain charge to mass ratio Q/M. The atoms are detected following the principle of a Faraday cup resulting in a current proportional to the number of atoms. A more detailed description can be found in [8]. By measuring the current one can obtain a time of flight spectrum (TOF) of the beam.

The two RGA detectors, Det1 and Det2 in Fig.2.1, are mounted in different ways. At Det2, the ionization area, focusing ring, quadrupole filter,etc. of the RGA lie in the plane of Fig.2.1 in one line with the direct beam direction. At Det1 the RGA is mounted perpendicular to the plane of Fig.2.1. The effect of different mounting orientations relative to the beam is not clear and has to be considered (Chap.6).

Chapter 3

Silicon as a Mirror

In this chapter the preparation of hydrogen passivated silicon (111) as an atomic mirror is described. This method has already been used in our lab [8]. At room temperature the pure silicon surface reconstructs to the (2×1) reconstruction, while after heating it falls into the (7×7) structure. This surface contaminates rapidly making it unuseful as a mirror. This problem can be addressed by hydrogenating the Silicon surface. This results in a Si(111)(1×1)H structure similar to the un-constructed silicon surface but covered by a mono layer of hydrogen. The helium reflectivity for this kind of surface and its lifetime are quite high. During passivation the surface is also smoothened resulting in an atomically flat surface separated by steps of atomic high. The method commonly used, called wet chemistry etching, is described below.

3.1 Etching Kinetics and Cleaning Process

3.1.1 Etching Reaction

For etching, a 40% ammonium fluoride NH_4F solution is used, which dissociates by the following reaction:

$$NH_4F_{(aq)} \overset{H_2O}{\longleftrightarrow} NH_{3(aq)} + HF_{(aq)}.$$

Hydrofluoric acid (HF) strongly dissociates. The solution has a pH value of $\approx$ 7.8. Note that the ammonium fluoride acts as a buffer solution for the hydrofluoric acid which is very useful since the etching process depends strongly on the pH value.

Every silicon wafer is covered by a 1nm thick oxide layer. To remove this layer and reveal the pure silicon structure the crystal is etched in the etching solution [11]:

$$R \equiv Si - (SiO_x) + HF \overset{-SiF_4,-H_2O}{\longrightarrow} R - SiF_3 + HF \overset{-SiF_4}{\longrightarrow} R \equiv Si - H$$

leaving a hydrogen passivated surface. R represents the silicon bulk.

The passivated surface itself is also attacked by the acid:

$$\begin{aligned} (R \equiv Si)_2 - SiH_2 + H_2O &\overset{OH^-}{\longrightarrow} (R \equiv Si)_2 - Si(OH)H + H_2(\uparrow) \\ (R \equiv Si)_2 - Si(OH)H &\overset{HF}{\longrightarrow} (R \equiv SiH)_2 + SiF_4. \end{aligned} \tag{3.1}$$

The etching process is purely kinetic and does not reach any equilibrium (except if the wafer is totally dissolved). The longer the silicon wafer is exposed to the solution, the more it is etched. The surface of the untreated silicon wafer is not perfectly flat. Different kinds of hydrated structures can be found. Some lie in a flat plane of passivated silicon and only have one hydrate sticking out and are thus called monohydrid. Others lie at the kink of a step only bound to the bulk by one bond but are bound by three hydrides and are therefore called trihydride. A complete description of all different types can be found in [11]. They can be ordered by their reactivity to the etchant. Roughly speaking, the more the hydride sticks out of the surface the faster it is etched. The lowest etching rate corresponds to a hydride that is part of a surface. Corners and single irregularities are etched fast while flat surfaces stay intact for a longer time. The difference in etching rates is of orders of magnitudes. Therefore the etching solution will tend to flatten or smoothen the silicon surface.

The silicon wafer is always cut along the (111) plane with a miscut angle θ. It turns out that the surface morphology changes for different miscut angles. Especially etched surfaces above and below a certain angle of about 0.1° greatly differ from each other. After the surface is smoothened by the etchant the reaction is governed by the ratio of two etch rates in relation to the miscut angle. One is the rate of etching one hydride at the flat surface while the other is the rate of etching a hydride at the corner of a step.

As shown in Fig.3.1 the silicon surface is atomically flat because kinks and single points reaching out of the surface are removed rapidly by the etching solution. Due to the miscut angle, steps of atomic height form on the surface. Those steps are made of dihydrides, which are etched, resulting in steps receding over the surface with etching time. The time it takes a step to move the average distance between two steps will be called $t_c(\theta)$. Depending on the ratio of the etch rates between dihydrides and terrace hydrides, a (terrace) mono hydride can be removed during t_c [12] [11] [13]. This results in a triangular shaped etch pit due to the triangular silicon lattice structure. If a step moves over an etch pit, this pit is removed resulting in a tip-shaped step structure (Fig.3.1).

If etch pits are nucleated faster (nucleation rate $> 1/t_c(\theta)$) than the steps move over the surface, the final structure will show a high etch pit concentration, probably also double or triple etch pits will be observable. The deeper an etch pit the faster it grows, a feature known as run-away reaction. This is due to pH inhomogeneities inside an etch pit leading to extremely roughened surfaces dominated by deep pits and V-shape structured steps.

If steps recede faster than etch pits are nucleated the final structure will show straight parallel steps (Fig.3.1) [14].

For high reflectivity, a big distance between steps as well as perfect terraces are important. Unfortunately the greater this distance, the more etch pits govern the surface. Etch pit formation increases non-linearly (run-away reactions) with decreasing miscut angle. A good compromise between big terraces and acceptable number of etch pits is a miscut angle of 0.1°.

Due to run-away reactions, the number of deep etch pits rapidly increases with etching time. Therefore a compromise between smoothing the surface by removing terrace irregularities and increasingly roughening the surface by pits has to be found.

As already mentioned, there is no steady state. The process is purely irreversible. The optimal etching time smoothens the surface while not creating to many etch pits.

3.1.2 RCA Cleaning

Before etching the silicon wafer one has to remove contaminations. Organic bound particles are hard to remove due to the strong $Si - C$ bonds. A

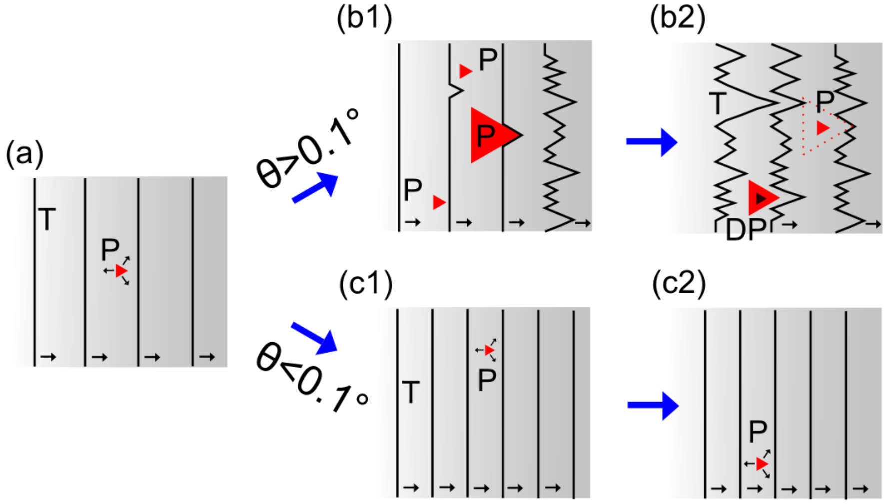

Figure 3.1: Etching kinetics depending on miscut angle θ. Receding steps (T) in arrow direction, etch pits (P), double etch pits (DP). **(b)** the etchant roughens the steps and more etch pits are nucleated possibly leading to deep run-away etch pits. **(c)** smooth terraces but a higher step density than in (b), new pits are removed by receding terraces resulting in parallel straight terraces [14].

layer of about 0.2 nm covers every new surface. To achieve good wafer cleanliness the RCA cleaning process is used. RCA [1] cleaning refers to a chemical mixture known for its properties for removing organic contaminants on silicon. The cleaning process can be split into two different sets of chemicals for organic (Type I) and inorganic (Type II) contamination. RCA-I is a $pH10$, $1:1:5$ mixture of 29 $\%_{wt}$ ammonium hydroxide (NH_3OH) solution, 30 $\%_{wt}$ hydrogen peroxide (H_2O_2) solution, and water [15]. The wafer is submerged into the solution for approximately 5 to 10 min at $60-80$ $°C$. The cleaning mechanism works as follows: the RCA-I solution slightly etches SiO_2 as well as Si. If dirt particles are undercut by oxide removal, electrostatic repulsion moves them away from the surface, while aqueous ammonia has a tendency to form complexes for example with $Co^+, Cu^{2+}, Fe^{2+}, Ni$ or Zn. At the same time a oxide layer (called chemical oxide, see [15]) forms on the pure Si which again is removed by oxidation [15]. The rate for removal of SiO_2 and growth of a oxide layer are roughly the same. Therefore only a small amount of Si is removed during RCA cleaning. However, the process results in a more rough surface where the roughness increases with temperature and time while the opposite holds for the cleaning efficiency.

Unfortunately metals like $Fe, Al, Ni,$ and Zn in the solution can form hydroxides which easily attach to the silicon wafer. The chemicals used are CMOS grade and therefore metal contamination is not a problem. In fact, even RCA-II is not necessary with this chemical grade.[15]. To give an estimate on

---

[1] RCA stands for Radio Corporation of America.

Si Wafer Properties

Diameter	100mm.
Type/Doping	N/Phos/Cz
Orientation	(111)±0.1°
Resistivity	$1 - 100\ \Omega cm$
Thickness	200 microns
Finish	Double Side Polish

Table 3.1: Properties of the used Silicon Wafers.

how crucial the cleanliness is: a 1 ppb Al containing RCA-1 solution can result in an surface covered by $\approx 10^{12} atoms/cm^2$ [15].

3.2 Experiment

3.2.1 Si Wafer

The properties of the silicon wafer used are summarized in table 3.1. The silicon wafers used are cut along the (111) plane by a miscut angle θ of $\pm 0.1°$. They are covered by a $> 1nm$ oxide and organic contamination layer. The big wafer are cut by a computer controlled dicing saw into smaller round pieces that fit into the rotor tip as described in [8].

3.2.2 Procedure

The process used follows the method described in [11]. It was already successfully done in our lab [8] and is now tailored towards surface quality. All cups used are made out of Teflon PTFE, rinsed by ultra pure 18 $M\Omega$ water and the chemical which will be used in it for several times. The silicon wafer is cleaned, then sonicated in methanol for 10min, isopropanol for 10min, and acetone for 5 min. It is then rinsed shortly with 18 $M\Omega$ water and submerged into the preheated 5:1:1 RCA-I solution at 75 - 80 °C for 5min. During that time the solution is continuously stirred. Only the water is heated and 2 min before inserting the wafer into the solution, ammonium hydroxide and hydrogen peroxide are added. This avoids evaporation of chemicals out of the solution making it less effective. After 5min the wafer is rinsed thoroughly by about 2 liter of 18 $M\Omega$ water and inserted into the etching solution. The etchant was purged with ultra high purity argon gas for at least 45min before etching to remove oxygen from the solution. Dissolved oxygen would disturb the etching process leading to deep etch pits. The solution is not stirred to avoid recontamination of the clean surface with already dissolved particles. A cap is placed on the cup containing the solution to inhibit evaporation. After about 11.45min the wafer is again rinsed by 2 liter of 18 $M\Omega$ water and inserted into vacuum after lees than 5 min. The time the wafer stays in air during the water rinsing is about 30 s to avoid contamination in air. The whole process is done in a clean fume hood.

Rinsing the wafer with water is critical especially between the cleaning and etching process since RCA residues would interfere with the etching kinetics resulting in deep etch pits. Also, the wafer is dried if necessary during the different processes with a jet of pure argon. This etching process depends on certain parameters like etching time, RCA cleaning time, and temperature. Those parameters have been tailored towards the flatness of the surface.

3.3 Results

An atomic force microscope (AFM) image of the etched surface can be seen in Fig.3.3. The image was obtained after about 15 min in air and 30 min in an Argon gas atmosphere for transportation. The resulting surface shows atomically flat terraces separated by steps of atomic height. Some dirt particles and/or oxidation can be seen on the surface probably due to the time in air. The flat structure covers almost the whole area of the Ø1 cm wafer.

Fig.3.2 shows a clearly over-etched structure. The number of etch pits is already high enough that even the described V-structure is being destroyed. Even multiple layers deep etch pits have formed. However, the atomically flat structure is still visible.

3.4 Conclusion

Although the silicon surface makes a good mirror in terms of reflectivity, the process is not very convenient. Several methods for improving the surface have been tried like O_2 plasma cleaning or RCA sonicating. Although both processes show better cleaning results they tend to roughen the surface too much, leading to more and deeper etch pits. The whole process of cleaning and etching takes several hours. Several hardly controllable factors can completely make the wafer useless. The wafer is very thin which makes it hard to hold with tweezers and therefore can easily brake. A crystal holder has been designed to address this problem, but still the wafer is very fragile. Sometimes during the

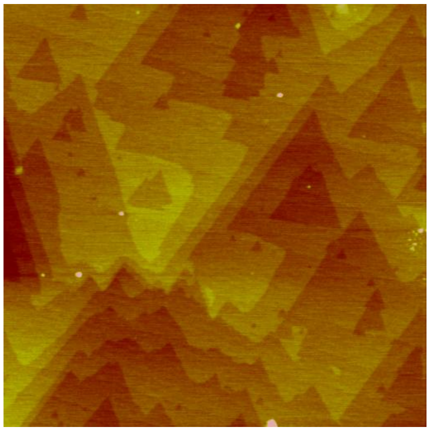

Figure 3.2: $2\mu m \times 2\mu m$ AFM image of a silicon surface. The surface is overetched that even the big etch-pits form on the surface almost destroying the typical step structure. Steps are separated by single atom steps of 2.5Å height.

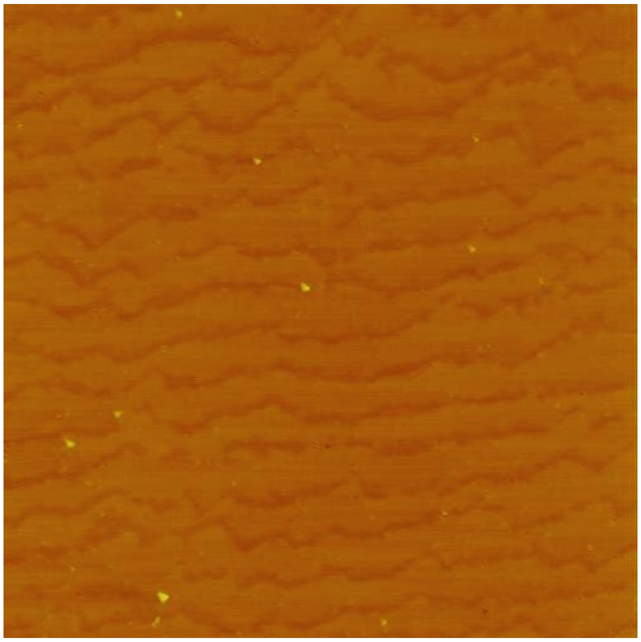

Figure 3.3: $4\mu m \times 4\mu m$ AFM image of a 11.45min etched silicon surface revealing the atomic height step structure. The steps form an angle equal to the miscut angle. Steps are separated by single atom steps of 2.5Å height.

sonicating process the wafers break, probably due to the creation of internal stresses during cutting.

Another problem appeared when using a different wafer set bought separately but with the same specifications. The atomically flat surface structure could only be observed on the wafers first bought and could not be repeated to the same quality with different purchases of the same kind making the results unreproducible. The process would have to be tailored for every new waver. Probably the reason is that a miscut angle of $\pm 0.1°$ describes the miscut error, it can also be less. If the actual angle is lower $0.01°$ the etch pit formation might dominate.

Besides the low reproducibility and the long preparation time the crystal lifetime is very short. After a few hours the reflectivity has dropped too much so that the wafer has to be replaced. Therefore the vacuum has to be broken, another crystal prepared, and vacuum has to be pulled again, requiring one day. For using the rotor as an independent source of cold high intensity beams of atoms and molecules, the silicon therefore is impractical although it works in principle.

A better mirror with a longer lifetime and shorter preparation time has to be found.

Chapter 4

Lithium Fluoride as a Mirror

4.1 Theory of Fracture

A possibility of receiving atomically flat surfaces might be cleaving a crystal by driving a wedge or knife into it. This was already done by Stern and Estermann in 1929 [16] observing diffraction patterns of molecular beams from a cleaved crystal. In order to understand the mechanisms behind this process a introduction into the theory of fracture and failure of material will be given. Of great engineering interest is the question of how things break, which can be answered quite well. On the other hand not much is known about the propagation of a crack through a material. To my knowledge the question of how things break, by means of crack development in time, and the path it takes are not fully understood yet.

Various computer simulations have tried to simulate fracture phenomena beginning at the atomic scale with braking of atomic bonds. The results often greatly differ from experiments possibly because the simulations critically depend on the chosen atomic potential. Weather or not a material is brittle or plastic is still an open question. Some materials shatter in parts when hit by a sharp wedge while others only tend to deform, thus more energy is required for cutting. In theory, a perfect brittle object would break into two pieces with two new atomically flat surfaces if the applied strain $\sigma = F/A$ reaches a certain limit (Fig.4.1a). Unfortunately this does not happen for reasons of plasticity.

In this chapter the basic theory behind failure of material will be given aiming towards cleaving material. Long derivations of formulas will be avoided and only qualitative explanations will be given.

4.1.1 Stress concentration

The point of fracture varies for different materials and geometries. From the view point of atomic bonds one cannot conclude about a materials's hardness. In fact, atomic properties have less effect on the point at which fracture occurs. More important, the strength of material depends on flaws and dislocations inside an object. As shown in Fig.4.1 different object geometries influences the stress field in different ways. In order to account for this, one can introduce the so called stress concentration factor

$$K = \hat{\sigma}/\sigma_{nom} \tag{4.1}$$

where $\hat{\sigma}$ describes the maximum local stress while σ_{nom} is the nominal applied stress. The concentration factor for a certain object geometry can be calculated by numerical and analytical methods or determined by experiments. For a elliptical shaped notch the intensity factor is given by

$$K = 1 + 2\sqrt{a/r} \tag{4.2}$$

where a is the notch depth and r the local radius [17] as seen in Fig.4.1b. As an example, assuming a notch with $a = 1mm$ and $r = 0.1mm$, the maximal occurring stress inside a material will be more than $K \approx 7.3$ times higher than the applied stress. In theory, when approaching atomic scales (≈ 1Å) the concentration factor can increase by orders of magnitude and even reach infinity in this model. Note that a perfect corner with zero radius results in an infinite large factor K. Thus, when applying stress to an object due to the stress concentration factor, one single flaw can increase the local stress and create a crack causing the material to fails.

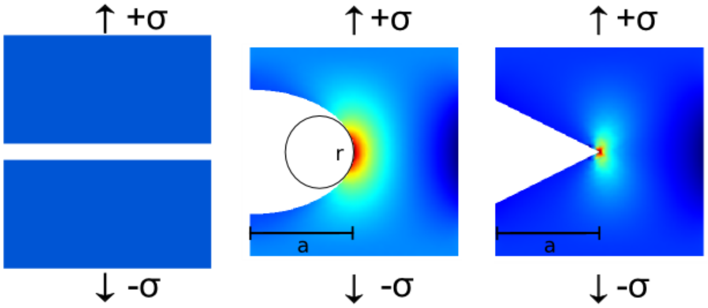

Figure 4.1: Failure of an object under applied stress σ as indicated by the black arrows. (a) Fracture in an ideal defect free and brittle material resulting in two new flat surfaces. (b) Stress concentration around an elliptic notch of length a and radius r and (c) around a zero radius notch. The colors represent internal stress in the arrow direction from red (high stress) to blue (low stress). The Color distribution is different for each figure. Highest stress increases from left to right.

4.1.2 Surface Energy

Obviously the difference between a cracked and uncracked body is the difference in surface area. On the atomic scale, the creation of surface requires breaking of atomic bonds and therefore requires a certain amount of energy. This is described by the surface energy $[\gamma_0] = J/m^2$ which is defined by the amount of energy necessary to create a surface per unit area. A system is always pursuing the state of lowest surface energy. In solids the surface energy depends on the surface orientation. The number of broken bonds and missing binding partner after separation can be a measure for the surface energy.

4.1.3 Energy Balance during Crack Growth

Whether or not a body is stable is determined by the question if there is a sufficient amount of energy to overcome the surface energy resulting in the creation of a surface. This is the main idea proposed by Griffith [18] in order to develop a crack propagation theory to find which conditions acting on an object cause crack propagation and result in failure. The principle of this so-called Griffith theory will now be explained briefly because it gives insight into the basic driving mechanism of crack growth. To calculate the point of failure one can simply use the law of energy conservation [19]:

$$\dot{W} = \dot{U}_{el} + \dot{U}_{pl} + \dot{T} + \dot{\Gamma}_0. \tag{4.3}$$

where $\dot{W}$ represents the external applied load, $\dot{U}_{el}$ is the internal elastic energy, $\dot{U}_{pl}$ is plastic energy, $\dot{T}$ is kinetic energy and $\dot{\Gamma}_0$ is the energy required to increase the crack area per time. All changes in time are directly related to changes in crack area A and Eq.4.3 can be written as

$$-\frac{\delta \Pi}{\delta A} = \frac{\delta U_{pl}}{\delta A} + \frac{\delta \Gamma_0}{\delta A} \tag{4.4}$$

where $\Pi = U_{el} - W$ is the potential energy of the system [19]. The kinetic term is neglected assuming slow material movement during crack motion. Eq.4.4 states the changes in elastic energy can only be done by changes in plastic energy or surface energy, meaning either plastic deformation or breaking. The left hand side of Eq.4.4 is also called the energy release rate $G = -\frac{\delta \Pi}{\delta A}$ which is the amount of energy released/consumed during crack growth per unit area. Only when this value is greater than the surface energy the crack can propagate and create a (flat) surface by consuming energy $\frac{\delta \Gamma_0}{\delta A}$. Depending on the plasticity of the material a rather big amount of energy will be consumed by plastic deformations $\frac{\delta U_{pl}}{\delta A}$ leaving surface defects behind. By using Eq.4.4 Griffith found a critical stress for an object σ_c at which it will fail if it contains an elliptical ideal crack (zero radius) of length a [18]. This is known as the Griffith criterion of fracture [17]:

$$\sigma_c^2 = \frac{2E\gamma_0}{\pi a}, \tag{4.5}$$

here γ_0 is the surface energy and E is the constant of elasticity.

4.1.4 Energy Dissipation

There are mainly two different mechanisms of energy dissipation during crack growth:

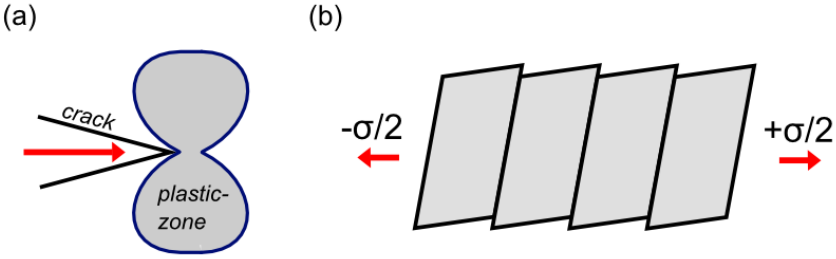

Figure 4.2: (a): shape of the plastic zone due to strain above the limit of elasticity of the material. (b): Slipping along crystallographic planes due to applied strain.

- **Dislocation Nucleation due to Plastic Flow**

  Most material exhibit plastic flow with increasing stress. At the tip of a crack the exerted stress increases by orders of magnitude due to the stress concentration factor Eq.4.2. The elastic strain cannot exceed the elasticity limit and therefore plastic deformation must dissipate the excess energy. This region surrounding the crack tip is called the plastic zone (see Fig.4.2a). It's shape and size can be calculated both by analytical [20] and numerical [21] methods and depends on different material properties and external conditions. Inside this zone, plastic yielding occurs resulting in the creation mainly of screw dislocations. Those screw dislocation appear due to material slipping along slip planes (Fig.4.2b). Slipping or gliding takes place along a consistent set of directions within these planes called slip directions. If a crack cuts such a screw component it will leave a step on the surface behind. Depending on the crack velocity, the time window in which a certain point on the lattice stays in the elastic zone (Fig.4.2) differs. The longer a point is in the plastic zone the more likely a dislocation can form and the more slipping can occur. Thus, the faster the crack the less dislocations are nucleated.

- **Dislocation Movement**

  Screw dislocations are dragged with the tip of a moving crack inside the plastic zone. This can lead to steps with a length in the *cm* range. This provides an energy dissipation mechanism resulting in an effective surface energy. Those dislocations are either created in the plastic zone or do exist in the lattice already. The amount of energy dissipated can be calculated [20]:

  $$\gamma_{eff} = \gamma_0 + \alpha\beta/L, \tag{4.6}$$

  where α is the dislocation density, β the energy dissipated by the work done on the dislocation, and L the crack length. The above equation shows that more work is required to cut a plastic than a brittle material because it will first deform before breaking.

4.1.5 Atomic View of Crack Propagation

A good understanding of crack velocity can be extracted from the atomic scale view of a crack propagating through a material. Note that in this model no plasticity appears, an ideal brittle material is considered. This theory is extracted from Michael Marder [22] and is interpreted for a cubic lattice. The translation from atomic to larger scale is not yet fully accomplished. However, it provides a good insight into crack motion on atomic scales. Con-

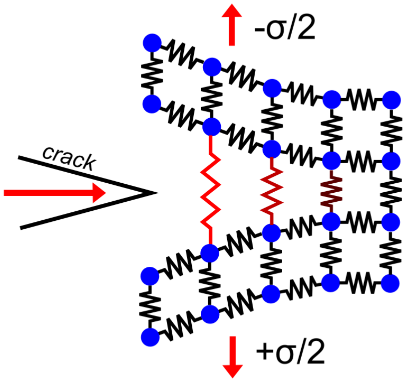

Figure 4.3: Atomic view of crack propagation.

sider a crystal lattice with one kind of atom. Chemical bonds are represented by springs in Fig.4.3.

The crack will advance if the atomic bond reaches a certain critical limit and breaks (see Fig.4.3). Before that no crack propagation is possible. After the bond breaks the released atoms will start oscillating. If the amplitude of the oscillation is high enough the next atomic bond will reach the critical length and break, resulting in a propagating crack. The breaking has to occur in the first quarter of the first oscillation period where the highest amplitude is reached. After that energy has already been taken away by vibrations through the neighbors in the lattice and the oscillation amplitude decreases. Therefore the external strain on the lattice has to be higher than the energy required to reach the critical bond length for every bond to be broken, else the crack will stop propagating which is called lattice trapping. The velocity at which the crack is propagating depends on the applied strain. The more excess strain energy the higher the oscillation will be. Thus, roughly the velocity increases with increasing strain. There is a so-called velocity gap where no crack propagation is possible because the energy is too low for breaking the next bond. A non zero temperature adds some kinetic energy to the atoms which can support bond breaking.

If the force on the lattice is too big the crack will reach a critical velocity. At this point, after the bond is broken, the oscillating atoms still have a sufficient amount of energy to break more bonds. This leads to the creation of multiple cracks running into the surface called branching. In that case the surface is very rough.

The crack will never be faster than the speed of sound. The speed of sound is the velocity of perturbations through a lattice. This speed depends on the spring constant which again depends on the number and strength of atomic bonds. Since the crack breaks bonds, the effective spring constant is lower and therefore the speed can not be as fast as the speed of sound. The motion of a crack can be categorized in three parts [23]:

- **Birth**:

  Crack propagation is not possible. Range reaches from 0 to 20% of the speed of sound.

- **Growth**:

  Crack motion is possible and stable resulting in a smooth surface.

- **Crisis**:

  Crack motion becomes unstable above a critical point. The crack velocity oscillates at high frequencies leaving branches of multiple cracks behind resulting in a very rough surface.

4.1.6 Cleavage with a Knife

Fig.4.4 shows how a knife forced into a material results in a crack. The sharp tip deforms the object resulting in a stress distribution with the heightest stress right in front of the tip due to the stress concentration factor (Fig.4.1). If this stress reaches the critical stress (Eq.4.5) a crack can form. Depending on the energy release rate $-\frac{dG}{dA}$ (Eq.4.4) and thus depending on the force applied, a propagating crack will form running along a crystallographic plane through the crystal. While the crack is advancing, the knife is moving into the crystal forcing the two halves apart, which adds to the stored elastic energy of the material and keeps the crack moving. The opening angle α of the knife is very important since it defines how strong the two crystal pieces are bent apart and therefore also determines the crack velocity.

4.2 Lithium Fluoride Single Crystal

Various diffraction experiments dating back to 1929 [16] have been done using lithium fluoride. Those experiments show good reflectivity for molecules like helium. The fact that diffraction patterns from a freshly cleaved surface were observed, leads to the conclusion that those surfaces are in fact atomically

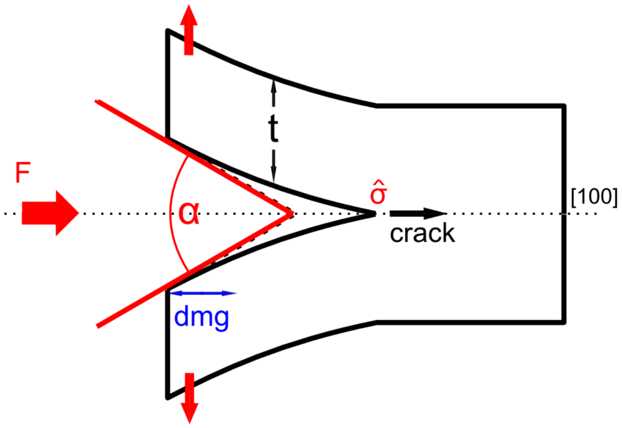

Figure 4.4: Knife with opening angle α forced into an object. This causes the two halves to bend. Due to the intensity factor the highest stress occurs at the tip in front of the knife marked by $\hat{\sigma}$. At this point the material will begin to fail. If the energy release rate is high enough a running crack will be created.

flat. One problem using passivated Si(111) as a mirror is the short lifetime due to contamination and oxidation and the long preparation time. With the choice of LiF one can avoid that problem which will be shown below.

4.2.1 LiF Crystal Properties

Lithium fluoride (LiF) crystallizes as a transparent face-centered crystal with a lattice constant of $g = 4.026$ [24]. The unit cell contains two Li^{+} and two F^{-} ions (see Fig.4.5). The bonding type is strongly ionic. Some properties of lithium fluoride are summarized in Tab.4.1. Due to the small ionic radii LiF has a very high lattice energy. Since the lattice energy is bigger than the hydratisation energy, LiF is hardly soluble in water.

Regarding the surface inertness one may believe that LiF, due to it's

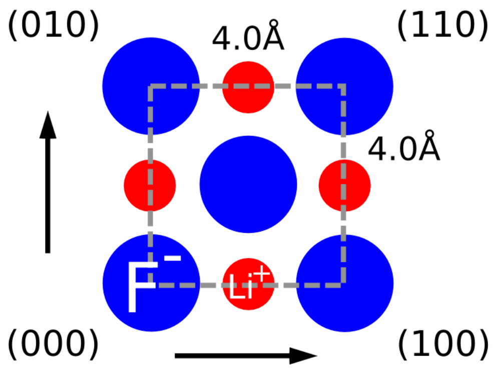

Figure 4.5: 4.026Å × 4.026Å unit cell of lithium fluoride.

Properties LiF

Space group	$Fm\bar{3}m$
Crystal structure	Cubic, NaCl type structure (FCC)
Coordination number	$Li[6]$, $F[6]$
Lattice parameter g [a]	$g = 4.026$Å
Density ρ [a]	$2.63905 g/cm^3$
Melting point [a]	$870°C$
Solubility in Water [a]	$0.27g/100g$ at $18°C$
Primary and secondary cleavage planes [b]	{100} and {110}
Primary slip plane and slip direction [b]	{110}, $\{1\bar{1}0\}$ and {100}
Surface Debye Temperature Θ_s	H-LiF[c] : $(415 \pm 44)K$
	He-LiF[d]: $(350 \pm 50)K$
Bulk Deby Temperature [e] Θ_b	$732K$

Table 4.1: Lithium Fluoride crystal properties. [a]:[24], [b]:[25], [c]:[26], [d]:[27], [e]:[28]

strong ionic bonding $Li^+ - F^-$, will show a low contamination, oxidation or other chemical reaction rate. Nevertheless, for a long time it was believed that a monolayer of water is adsorbed on freshly cleaved *LiF*. In fact, various analyzation techniques such as mass spectroscopy now seem to confirm that virtually no hydroxide or water layers are formed on the surface [10] [29]. Only under extreme conditions such a layer can form [29], but can be removed by thermal annealing. The inertness therefore makes *LiF* a good choice in terms of crystal lifetime.

4.2.2 Cleaved Surface Structure

The LiF (100) surface remains the ideal (1×1) structure with little significant spacial displacement. A cleaved surface shows two different types of steps [30], called cleavage steps, of heights reaching down to atomic dimensions. One type of step is always perfectly straight and aligned with crystallographic planes $\{100\}$. Those steps are also called slip steps. The other type is not necessarily straight and does not follow crystallographic directions. Generally those steps are radiating from the corner in which cleavage was initiated. Their direction varies over the crystal following the way the cleavage front is advancing.[30]

As shown in Tab.4.1 the primary cleavage lies in $\{100\}$. The slip planes lie in $\{110\}$ and $\{1\bar{1}0\}$ with an $\{100\}$ slip direction [1].

---

[1] Square brackets describe directions, round brackets describe planes perpendicular to the given direction (for example the (010) plane is the plane perpendicular to the [010]

Furthermore, so-called V-shape structures cover the surface. A V-shaped tip is formed by a cleavage step in the cleavage direction and a slip step along the slip system direction [30]. The V-shape structure size depends on the angle between the two steps and therefore varies over the crystal area. Less commonly cleavage can also occur on the secondary cleavage plane in combination with the secondary slip system.

The structure just explained will be shown on actual cleaved *LiF* in the experimental section.

4.3 The Cleaving Apparatus

4.3.1 Conclusions from Theory

To initiate cleavage a knife is used to nucleate a running crack through the material, creating two flat surfaces. Force is applied on the knife and if the strain in the material at the knife tip reaches the critical stress (Griffith criterion, Eq.4.5) the crack will propagate, assuming that the energy release rate overcomes the surface energy (Eq.4.4). The sharper the blade, the higher the concentration factor, and the faster the critical stress is reached. Driving the knife into the crystal forces the two pieces apart, resulting in elastic energy stored in the material. Depending on the knife opening angle the strain energy is different. If the angle is not optimal the crack probably gets trapped and the crystal brakes or the crack branches.

---

direction) and curly bracket { } represent all permutations of the given direction or plane ({100}: 100, 010, 001, $\bar{1}00$,...)

The following provides a summary about important requirements on the cleaving apparatus.

- The crystal should always be halved. The ratio of maximum stresses in both parts of the halved crystal during cleavage is

  $$\frac{\hat{\sigma_2}}{\hat{\sigma_1}} = \left(\frac{t/2+\delta}{t/2-\delta}\right)^{\frac{3}{2}}$$

  where t is the thickness of the crystal and δ the offset of the knife from the center. This formula can be calculated by the model of simple cantilever beam dynamics [31]. If a 4 mm thick crystal is cleaved 0.25 mm away from its center ($t/2$) the ratio of maximum stresses becomes $\frac{\hat{\sigma_2}}{\hat{\sigma_1}} = 1.46$. This imbalance can cause the crack to sheer out of line resulting in a break off of the thinner piece. The stress ratio is bigger for thinner crystals. A thickness of 2 mm with the same alignment error would result in an stress ratio of 2.15. Thus, aligning the blade in the center becomes more and more important with thinner crystals.

  In order to cleave from a larger slab at thicknesses above about 1 cm the piece can still be cleaved without halving it.

- The blade should be as sharp as possible, leading to a small blade tip radius ρ and making less force necessary to initiate cleavage due to the intensity factor $K \propto \sqrt{\rho}$ (Eq.4.2).

- The blade should touch the crystal at only one point to avoid multiple crack initiations on different planes (if misaligned).

- Short sharp hits with a small hammer should be used. The force should be enough to drive the crack above the critical velocity and to avoid the crack becoming stuck. The force should be kept as low as possible. If too much force is applied, the crack starts branching, creating more steps, cleaving on other planes, or even breaking the piece due to stress imbalances.

- The blade should be aligned closely to the (100) cleavage plane to avoid cleavage of different planes such as a different $\{100\}$ or the secondary (110) plane.

4.3.2 Implementation

Various cleaving devices in-situ as well as ex-situ have been designed [32] [33] [34]. Due to the inertness of the used crystal a method outside vacuum can be used. Most devices use a blade which pushes the crystal against an anvil. The blade can be driven by simply using a hammer [34] or pressing against a blade extension [33]. Fig.4.6 shows the actual design. The crystal is placed in a groove on the bottom acting as an anvil (a in Fig.4.6). Besides the groove, there is a scale for aligning the crystal such that the blade halves it. The blade (b) is clamped with two screws between an extension rod that guides the knife. The blade can easily be removed for exchanging or sharpening it. The blade is made out of hardened stainless steel C400. The knife angle is 12° as a compromise between blade sharpness and material strength to avoid bending or breaking. After a number of uses the knife is sharpened with

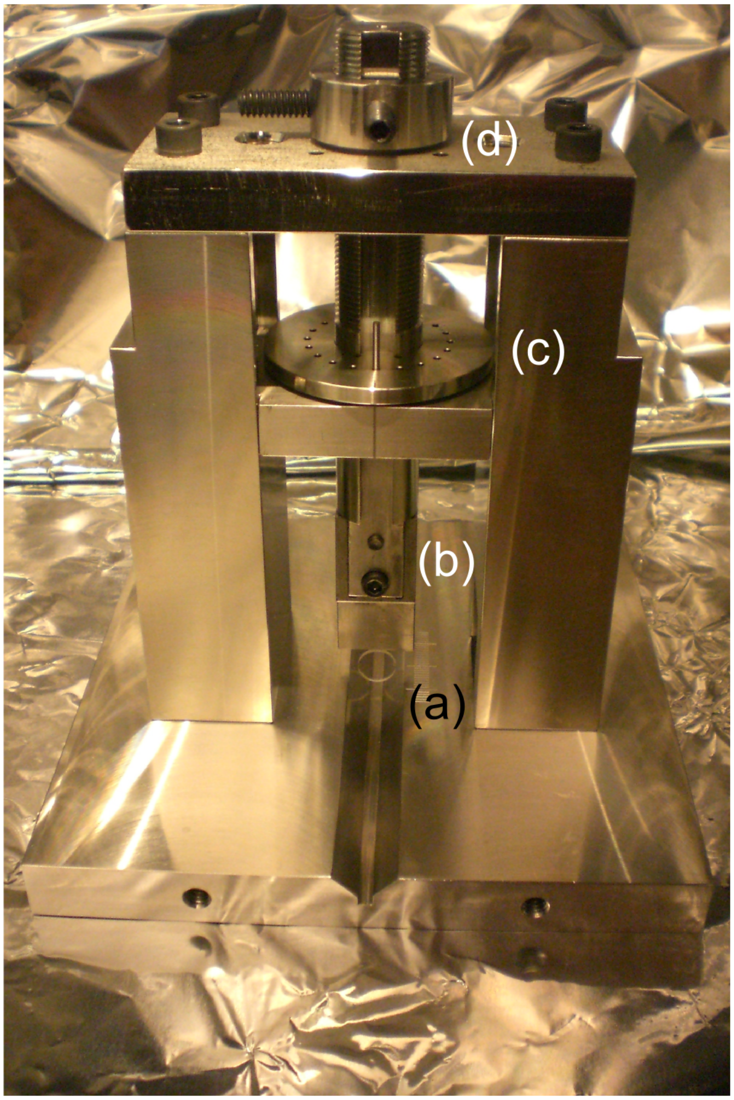

Figure 4.6: Picture of the cleaving apparatus as described in section 4.3.2. The diameter of the shown crystal is Ø10mm.

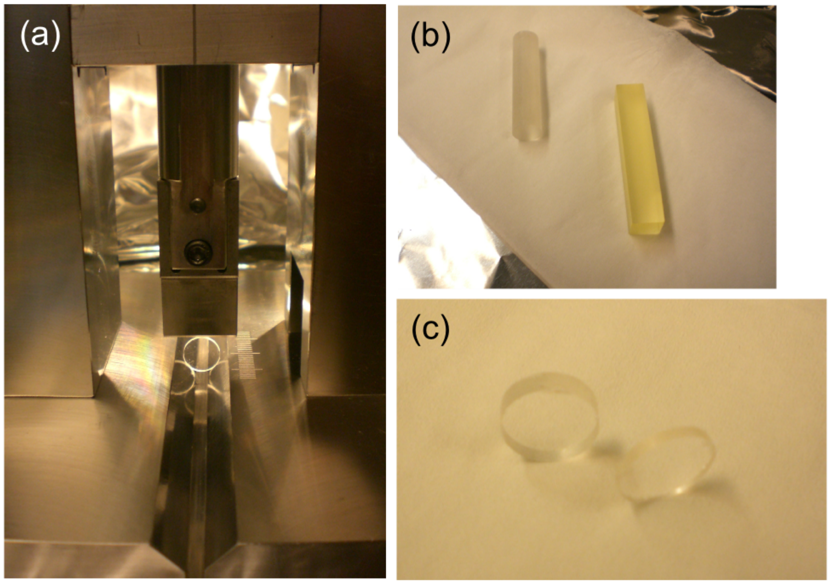

Figure 4.7: (a) magnification of the cleaver. (b) two different LiF crystals from which thinner pieces are cut (No.2 and 3 from Tab.4.2) (c) crystal pieces after cleavage. In all images the diameter of the crystal is Ø1cm.

a whetstone. During sharpening the knife angle has been varied for better cleaving. This sharpening method is not very accurate in terms of the knife angle. However, it is critical for cleavage as seen in Fig.4.4. Therefore there is potential for improvements as described in Chap.7. The guiding rod has two grooves so it can be guided by an alignment plate (c). The top of the rod is threaded and a ring (d) can be screwed on it. The ring has two set screws for clamping it down at the right position. By turning the stopping ring, the blade can be lowered till it touches the crystal. Then the crystal is removed and the ring is turned further to set the depth the knife can move into the crystal. The stopping ring is threaded by 36 threads per inch. Thus, by turning the stopping ring one turn the blade will stop after advancing about $1mm$ into the crystal. When cleaving has been initiated and the crack halves the crystal the ring (d) hits the stopping plate preventing the knife from driving too deep into the crystal destroying the fresh surface. For aligning the blade parallel to the cleavage plane the alignment plate (c) is used following the principle of the Nonius Scale. On the alignment plate holes are drilled on a circle separated by $18.1°$. The platform underneath has holes drilled also on a circle but $18°$ apart. Thus only one combination of holes can be positioned axial symmetric, a pin is inserted to keep this position. Depending on the combination of aligned holes the alignment plate and through the guiding the blade can be turned by $\pm 0.1°$ allowing exact alignment. The advantage of this design is that the current alignment plate can be easily replaced by a different one with different hole positions allowing it to increase or decrease the angular alignment precision. The current plate used reaches from $-0.9°$ up to $+0.9°$ in $0.1°$ steps.

All parts except the knife are made out of stainless steel. The device is specially design to be very rigid so that forces are directly translated into the crystal. The crystal is cleaved by hitting the top of the rod (d) with a small hammer.

4.4 Results

Different lithium fluoride crystals have been used (Tab.4.2). They are either round or square shaped rods, and the purity as well as the growing method varies. The following sections will deal with the results obtained for each type of crystal.

Lithium Fluoride Crystals

No	1	2	3	4
Manufacturer	Superconix [35]	MaTecK [36]	REXON [37]	Argus Int. [38]
Length	50mm	50mm	50mm	100mm
Face ($< \pm 0.2mm$)	(10mm)^2	Ø10mm	(10mm)^2	(10mm)^2
Miscut	±0.5°	±0.1°	NA	±2°
Purity	$> 99.995\%$	$> 99.9\%$	γ hardened	-
Growing method	vac	vac	vac	Kyropoulos

Table 4.2: Overview of LiF crystals used in the experiment. 'miscut' column describes the parallelism of the face to the (100) cleavage plane.

4.4.1 Pure Lithium Fluoride

The first results were obtained from a square $10 \times 10 \times 50\ mm^3$ crystal with the (100) plane parallel to the face by ±0.5° (No.1 in Tab. 4.2). To initiate cleavage the knife had to be hit many times, causing the knife to penetrate into the crystal about $1 - 2\ mm$, damaging the edges as well as the fresh surface. From the 5 cm long piece about 8 mm thick pieces are cleaved off. Below about 8 mm alignment becomes critical and the pieces always have to be halved. It is possible to cleave crystals to a thickness of about 2 mm but alignment is very critical at that thickness and the error rate becomes high. Fig.4.8 shows a picture of a cleaved surface taken by an optical microscope. The crystal actually is transparent. The orange tone comes from different filters used to obtain a better contrast. One can see big cleavage steps on the order of 10ths of microns running along the direction of the propagating crack. Along those bigger steps smaller steps also stretch over the surface reaching down to atomic height. Those features are not visible by an optical microscope.

Fig.4.9 shows an atomic force microscope (AFM) image. It turns out that getting an image is hardly possible. The reason is a common problem of imaging cleaved ionic crystals. During cleavage surface charges are left on the surface. The interaction between surface charges and AFM tip make it almost impossible to receive a rough image. To reduce those charges one can use a standard γ ionizer. The γ radiation ionizes the surrounding air which then neutralizes surface charges. After treatment with an ionizer and resting in air it is possible to obtain some higher resolution images. The interaction between the ionized air and the charged surface is not clear. Probably the high contamination of Fig.4.9 corresponds to former surface charges. Despite the radiation, the surface probably still has charges indicated by horizontal lines distorting the image. Due to the problems of imaging, it is not clear if truly atomically flat surfaces are created and if they are free of contamination.

The cleaved crystals are inserted in the holder, then into the chamber. Moving the rotor to the reflecting position (R in fig.2.1), the reflected signal is measured. With these crystals only a diffuse signal could be recorded. Elastic reflection was not detectable.

One reason for the low reflectivity is suspected to be related to the plasticity of LiF. Ionic crystals are commonly expected to be very brittle and therefore should show excellent cleaving results. Various publications have reported that old crystals used to show good cleaving results while recently

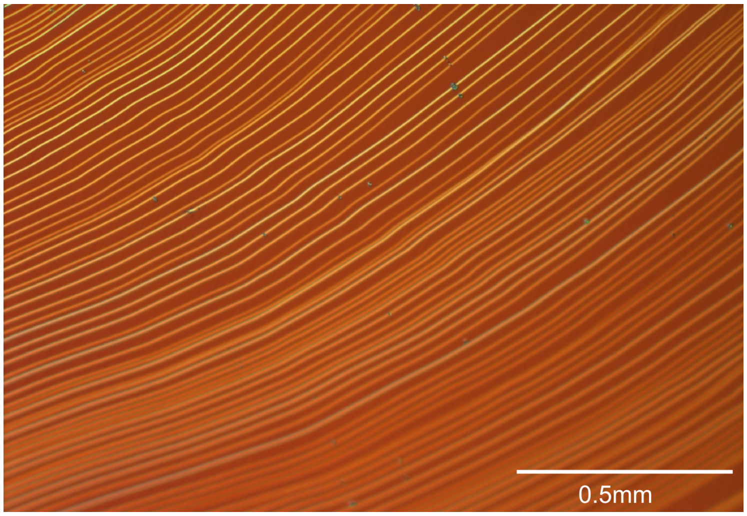

Figure 4.8: ×20 magnification of cleaved LiF taken by an optical microscope.

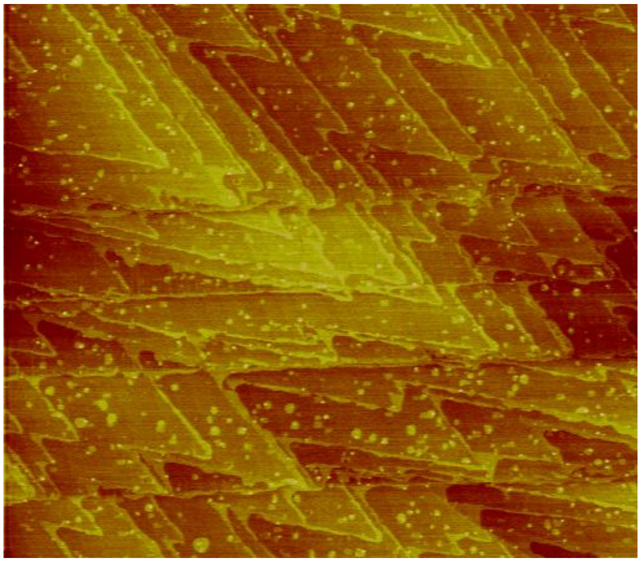

Figure 4.9: $4\mu m \times 4\mu m$ AFM image. Bad image quality probably due to charges indicated by the 'glowing' effect of steps. The surface was radiated by ionizing γ radiation to reduce charges. About 1hr after preparation.

bought ones were hardly cleavable [10] [39]. We expect that the reason might be the different crystals growing methods used. Today single crystal are commonly grown in vacuum, while earlier they where grown in air. Growing in vacuum leads to very pure (see Tab.4.2) crystals with little lattice defects and almost perfect structure. Air grown crystals on the other hand show many impurities and lattice defects. We suspect that these defects, resulting from trapped air and lattice vacancies cause a higher stress concentration (see Eq.4.2).

There is a certain stress required in a crystal to create slipping. If the impurity concentration is high enough, the stress concentration factor might cause the crystal to break before slipping can occur. That little elastic energy is spent on plastic deformation (Eq.4.4) and a perfect (low step density) surface can be formed. In fact, it turns out that pure LiF is plastic while impure LiF on the other hand is very brittle. The strongly damaged edges as well as the many hits the knife needs to nucleate a crack confirm that a big amount of elastic energy is wasted in plastic deformations.

[40] also suggests that impurities (especially magnesium) of air-grown crystals causes brittleness by increasing the required critical shear stress for slipping by an order of magnitude. In the atomic picture of crack motion (Sec.4.1.5) impurities such as magnesium ions might act chemically as a catalyst reducing the critical bond length in the crystal making advancing a crack easier.

4.4.2 Kyropulous Air Grown Lithium Fluoride

Air grown crystals (so-called Kyropulous method) also were examined (No.4 in Tab.4.2). We expect them to show roughly the same amount of impurities, and therefore brittleness, as the crystals used in earlier He-LiF diffraction experiments. The cleavability is similar to the radiated crystals but they exhibit multi-faceted surfaces, while the other crystals (No.1-3) always showed a single facet. We expect those facets to come from grain boundaries of the crystal resulting in cleaved (100) planes tilted to each other along those boundaries. This unnecessarily reduces the reflectivity of the surface since not all specularly reflected atoms will hit the detection region. The imperfection of the crystal lattice has its origin in the growing method which does not result in a good crystal structure. This makes the results from different air grown crystals or even different points on the same crystal unpredictable.

4.4.3 γ Hardened Lithium Fluoride

As mentioned in the above section, pure crystals do not show good cleaving results. Therefore vacuum grown crystals (No.3 in Tab.4.2) radiated with γ-rays from an Co-60 source have been purchased. Ionizing radiation is known to create so-called F-centers or color centers in the lattice. An F-center is a lattice vacancy in an ionic crystal which is missing an anion. This vacancy can be occupied by electrons. Those electrons can absorb light causing the crystal to change its color. In lithium fluoride the F-centers absorb visible light resulting in a yellowish crystal (instead of transparent). Further radiation can even change the color to amber or black. As shown in [39], γ radiation from a Co-60 source with a flux of 4×10^5 r/hr can increase the resolved shear stress by a factor of over 14.

The crystal used is listed in Tab.4.2. It shows a yellowish color as shown in Fig.4.7c. Cleaving can be easily achieved by one or two sharp, light taps on the knife. Crystal thicknesses of below 0.5 mm can be achieved easily with one tap, allowing for a total preparation time of a few minutes. When cleaving to a thickness of about 0.25mm alignment becomes very critical. The edges show far less damage indicating that the crystals are single-faceted with low plasticity. An AFM image as well as a height profile is shown in Fig.4.10 and Fig.4.11. An image can immediately be obtained after 1 hr of storage in argon. Surface charges were not observed on the scale of Fig.4.10. The height profile clearly shows the expected cleavage steps. In this image cleavage and slip steps run close to parallel resulting in long stretched V-shaped structures. Terraces of μm size can be observed. The structure obtained by cleaving is clearly comparable to AFM height profiles of other cleaved crystals such as potassium bichromate [41]. (Unfortunately no height profile of cleaved LiF on this small scale could be found.) The radiated crystals clearly show the best cleaving results. Fig.4.12 shows a picture of a cleaved piece. Some cleavage steps following the crack direction over the surface can be seen by eye. The surface is a single (100) facet, showing good light reflection which can also indicate good atomic reflectivity. The piece has a thickness of $0.49mm$ which can now be achieved with almost every attempt.

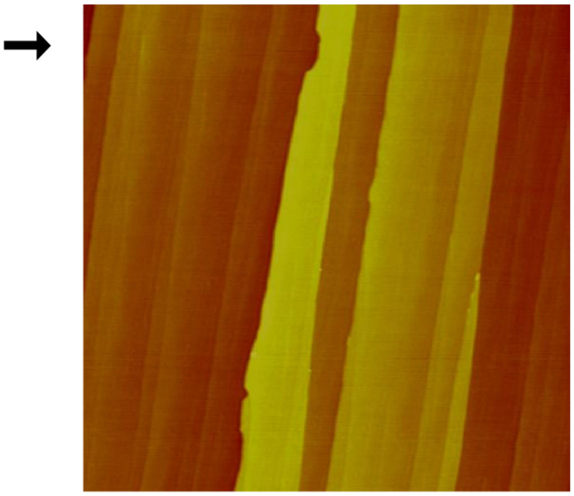

Figure 4.10: $10\mu m \times 10\mu m$ AFM image of cleaved LiF after about 1hr storage in an argon atmosphere and 1hr in air. The yellow LiF was used. Black arrow indicates the measured height profile in Fig.4.11.

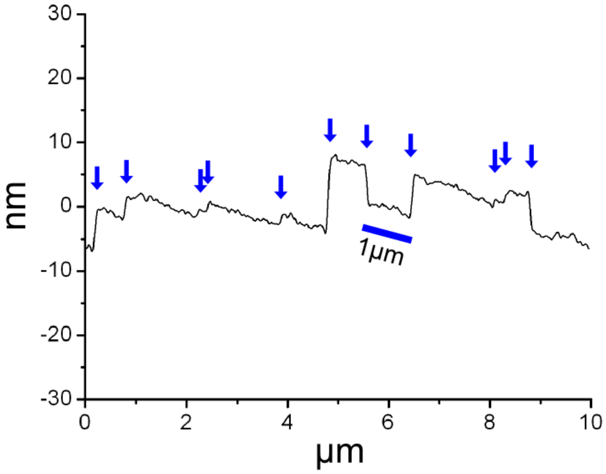

Figure 4.11: Height profile of a freshly cleaved surface taken by the AFM measured along the line indicated by the arrow in Fig.4.10. Blue arrows mark cleavage steps. The whole surface appears to be tilted for experimental reasons.

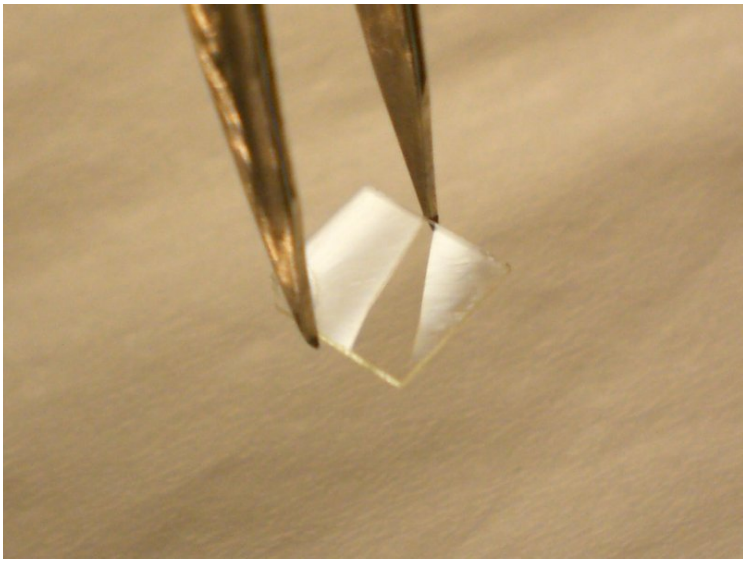

Figure 4.12: Example of a freshly cleaved $10mm \times 10mm$ γ hardened crystal which can be achieved with almost every attempt. The piece has a thickness of $0.49mm$. Note that it is a single faceted surface showing good light reflection which can be an indication for good reflectivity.

Chapter 5

Rotor Improvements

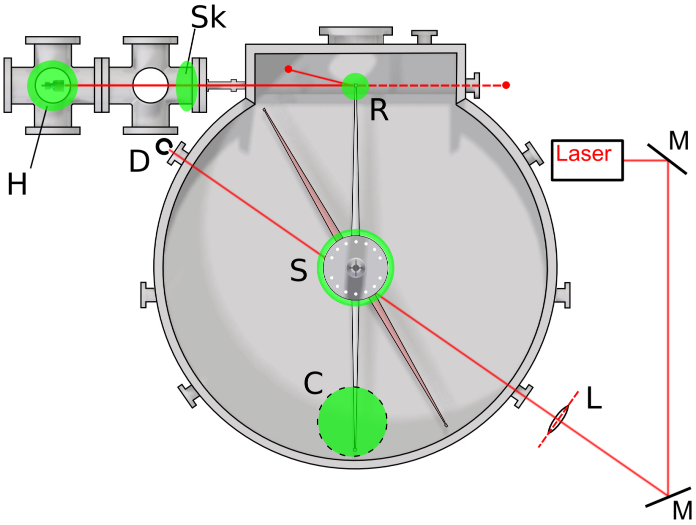

Figure 5.1: Overview of improvements on the rotor experiment marked green. H: new cryogenic nozzle holder, Sk: new skimmer mount, R: new crystal and holder, S: new spindel, C: cryo-trap and the laser system (D: Photodetector, L: Lense) for detecting resonance frequencies.

As shown in Fig.5.1 various changes have been made by our group for improving the experiment. New crystals as well as different holders are used, allowing for longer life and shorter preparation time, as described above. A new cryogenic nozzle holder for cooling the nozzle to LN_2 temperature has been built. A cryo-trap for faster pumping speed, allowing for a longer crystal lifetime has been built. Also, the skimmer mount has been improved. A new spindle with a lower mass and moment of inertia, making it possible to spin faster, has been installed.

Since the rotor is spinning at high frequencies, the rotor material is exposed to high stresses. One has to make sure that no material limit is reached while the rotor is spinning. Material failure would be fatal due to the high kinetic energy. Also special care has to be taken on rotor resonance frequencies which could amplify up to failure. Since the rotor contains a new lower mass spindle, different holder and crystals, the behavior at high speeds has to be reconsidered. Therefore a laser system has been set up (see Fig.5.1). A laser beam is focused through a lens onto the spindle (S) in a way half the light passes and reaches a detector. If the spindle reaches a resonance frequency and begins vibrating the detector will detect a change in intensity. Furthermore, the signal is analyzed in terms of intensity of resonance frequencies at various rotor speeds. Simulations have been carried out to compare the experimental results. It is assured that the stress in the spinning rotor is more than an order of magnitude lower than the yield tensile strength. The simulations agree with experiment. The rotor can now be operated at up to 48Hz which corresponds to a tip velocity of 150.7 m/s. Additionally, the laser detector signal is implemented in the rotor control program. If the root mean square (RMS) amplitude of the detected light reaches a certain value to rotor turns off as a safety precaution.

Chapter 6

Results

In this chapter the first results of reflecting helium from a cleaved LiF crystal from a standing and moving mirror are presented. The measurements provide a proof of principle, although all data presented is preliminary and further exact measurements have to be done.

As described in chapter 2, the RGA detector outputs a voltage proportional to the number of detected atoms. Therefore, only relative signals are relevant. The direct beam detector is mounted horizontally while the other is mounted vertical (see section 2.7) and the effect on the measurement is not clear. In order to make the direct and reflected beam signals measured with different detectors comparable, the signal to noise ratio S/N is used. Here, the noise amplitude is defined as $2 \cdot \sigma$, where σ is the standard derivation $\sigma^2 = \langle X - \langle x \rangle \rangle^2$. Brackets $\langle x \rangle$ represent the arithmetic mean. Thus, 68.3% of the measured signal lies in the $\langle x \rangle \pm \sigma$ region.

6.1 LiF Reflection Signal

Fig.6.1 shows the reflection of helium of a 30:70 He-Ne mixture with a nozzle backing pressure of 60 *psi*. γ-ray hardened crystals of about 0.5mm

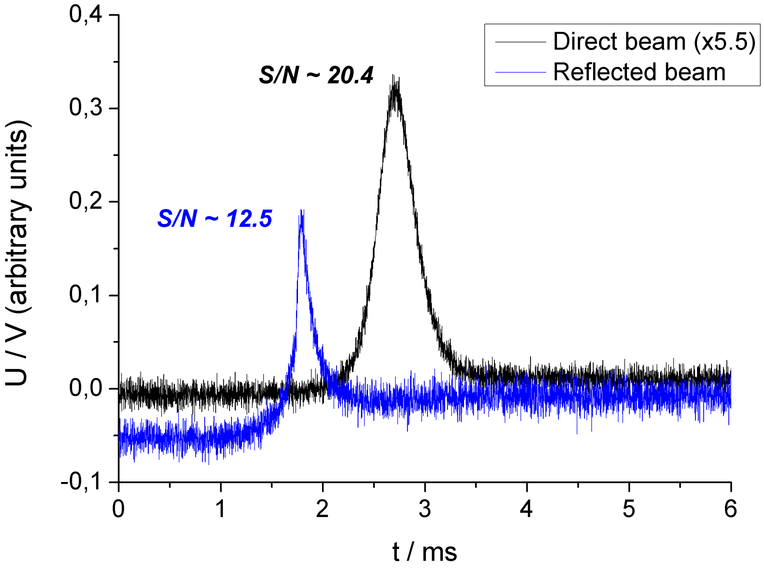

Figure 6.1: Helium reflection with a 30:70 He:Ne mixture from (100) LiF compared to the direct beam. 'S/N' stands for signal to noise ratio. The direct beam data has been multiplied by a factor of 5.5 for comparison.

thickness are used. The reflected beam appears earlier than the direct beam because they follow paths of different lengths. The background signal is lower before than after the peak, which corresponds to the thermal beam expanding into the rotor chamber, while the super-sonic beam is detected (this makes the reflected beam signal slightly asymmetric as well). The direct beam signal barely shows this effect because a Ø5 mm aperture separates the direct beam detector from the main chamber. For comparison, the direct beam signal is multiplied by a factor of 5.5 to make the noise approximately the same for both signals. A better comparison would be the signal to noise ratio (S/N).

The direct beam shows $(S/N)_{direct} \approx 20.4$, while the reflected beam gives a S/N ratio of $(S/N)_{refl} \approx 12.5$. Based on the signal to noise, the reflected beam appears a factor of

$$\frac{(S/N)_{direct}}{(S/N)_{refl}} \approx 61\% \tag{6.1}$$

lower than the direct beam.

The distance between nozzle and direct beam detector is $(1.36 \pm 0.02)m$. The nozzle responds with a delay of $\Delta t = 40\mu s$ due to the driving electronics. The direct beam pulse arrives at $(2670 \pm 14)\mu s$, with a FWHM of $\Delta t = (424 \pm 60)\mu s$. The beam velocity is calculated to

$$v = (503 \pm 10)m/s, \tag{6.2}$$

which corresponds to a 30%:70% He:Ne mixture. By using Eq.2.7, it follows for the speed ratio S:

$$S_{direct} = 15.5 \pm 2.2 \tag{6.3}$$

With Eq.2.6 the temperature of the beam becomes:

$$T_{direct} = (790 \pm 233)mK. \tag{6.4}$$

For the reflected signal one gets:

$$S_{refl} = (24.4 \pm 3.0) \text{ and } T_{refl} = (323 \pm 80)mK. \tag{6.5}$$

The temperature of the reflected beam Eq.6.5 lies in the expected mK range. The direct beam temperature Eq.6.4, on the other hand, is noticeably high.

The difference most likely comes from the Ø5 mm aperture separating the direct beam detector from the main chamber and the pumping system. In this separated region the background gas pressure is higher and the direct beam is heated due to collisions.

6.2 Spinning the Rotor

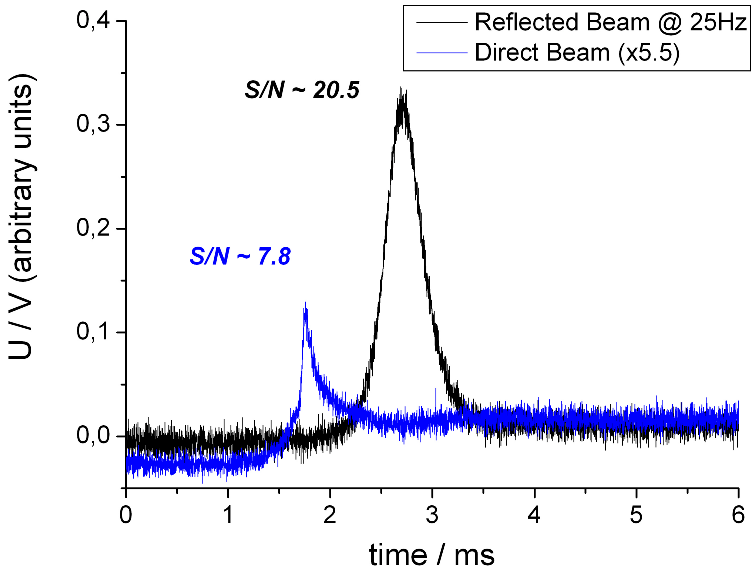

Figure 6.2: Helium reflection from a 30:70 He:Ne mixture from (100) LiF compared to the direct beam while the rotor is spinning at 25Hz. The direct beam data has been multiplied by a factor of 5.5 to make the signal measured with different detectors comparable.

Fig.6.2 shows the first reflection results obtained at 25Hz. This experiment was only a proof of principle and was not intended to spin at high frequencies. The rotor can spin faster but the masses of the two crystals on opposing sides of the rotor would have to be balanced fist. The signal to noise ratio of direct and reflected beam becomes:

$$\frac{(S/N)_{refl}}{(S/N)_{dir}} \approx \frac{(7.8)}{(20.5)} \approx 38\%. \tag{6.6}$$

The same nozzle settings and gas mixture as in the above section is used. The initial beam velocity is $v = (503 \pm 10) m/s$, corresponding to a 30%:70% He:Ne mixture. The rotor is spinning at $(25.000 \pm 0.001) Hz$, thus, the mirror velocity is $(79.122 \pm 0.003) m/s$. Eq.2.1 leads to the velocity of the reflected beam. The final beam velocity should be

$$v_f = 344\ m/s.$$

Assuming the moving mirror does not heat the beam significantly more than the standing mirror, the temperature of the slowed, reflected beam is given by:

$$T_{refl,25Hz} = (323 \pm 80)\mathrm{mK} = T_{refl}.$$

Due to the small reflection signal, the influence of the thermal beam becomes significant, resulting in an asymmetric signal shape. This makes the signal non Gaussian. Thus, Eq.2.6 and Eq.2.7 cannot be applied and the temperature cannot be calculated in this model by measuring the FWHM Δt.

6.3 Crystal Life-time

The freshly cleaved surface stays in air for less than 5min before it is inserted into the vacuum chamber. After 1h, at a main chamber pressure of about 10^{-7} torr, with a nozzle cooled to LN2 temperature, the experiment is started.

The reflected signal, after 130min of measurement with the RGA filament turned on, decreases to about (94 ± 4)% compared to the reflection before the measurement. Crystals have already been used up to 6hours. In contrast, silicon shows a rapid decrease in reflectivity when the RGA filament is on, while the RGA filament does not seem to be a major cause of reflection loss for LiF. (Previous experiments [8] show a reflection loss of 50% for silicon after about 25min.)

6.4 Closing of Diffraction Channels

With the new mirror material we expect to benefit from a certain scattering effect called rainbow scattering.
Rainbow scattering describes the phenomenon of strong maxima appearing in the classical scattering probability as a function of scattering angle. The name comes from classical optics where light scattered from raindrops has a strong maximum at a certain scattering angle. Rainbow structures are characteristic for surfaces with a high corrugation amplitude compared to the incoming particle's wavelength. Table 6.1 shows *He-LiF* diffraction probabilities for different diffraction channels [42]. This clearly confirms a high corrugation amplitude for LiF due to it's strong ionic character. For an incident angle of 40° the diffraction probability in the (2,2) channel is even 239 times higher compared to (0,0) order diffraction. This makes LiF an ideal material for diffraction

studies, since only little intensity is lost in specular reflection. Unfortunately, in this experiment higher order diffraction is lost and not detected.

At 297K the surface lattice constant of LiF is 4.02Å [43] corresponding to a crystal momentum of $k_{LiF} = 1.56$ 1/Å. An incoming particle is diffracted if the scattering condition $\Delta K = G_{n,m}$ holds (see section 2.5.1). Therefore the second diffraction channel $G_{\pm 2,\pm 2}$ is closed, if the incoming particles momentum is below $k < 2 \cdot k_{LiF}$, where the factor of two corresponds to the second order diffraction. Thus, a particle with a velocity below 3.12 1/Å $= 496 m/s$ cannot undergo second order diffraction.

Thus, we expect an increase in specular reflection intensity when the second order diffraction closes. This effect should compete with a problem we call the fanning effect: Let the FWHM of the incoming beam be $\Delta t = 424\mu s$ (section 6.1). On this time scale, spinning at 25Hz, the rotor has turned by 3.8°, distributing the reflected beam over at least 7.6°, resulting in a lower signal at high crystal velocities. This effect is a major disadvantage resulting in a great loss as shown previously with a Si(111) mirror [8].

Fig.6.3 shows the detected reflection intensity at different rotor fre-

Diffraction Probabilities $P_{nm} \cdot 10^3$

Diffraction Channel	(-3,-3)	(-2,-2)	(-1,-1)	(0,0)	(1,1)	(2,2)	(3,3)
$P_{nm} \cdot 10^3$	0.7	20.7	1.1	3.3	1.1	20.7	0.7

Table 6.1: Diffraction probabilities $P_{nm} \cdot 10^3$ for a room-temperature supersonic helium beam scattered from 80K (100) LiF along the 100 direction with an incident angle of 0° taken from [42].

quencies. In fact, a slight increase in reflection intensity was observed during the run. The reflection between 10 to 15Hz even reaches the intensity of a standing mirror. This might indicate that a big fraction of atoms is diffracted into higher order as long as the 2nd order diffraction channel is opened.

Data of a previous experiment [7] using Si as a mirror, fitted by an exponential decay, is shown along with the LiF results. The LiF and Si data are normalized to the corresponding reflection signal of a standing mirror (0Hz). The effect of closing diffraction channels is not observed for silicon. Therefore the decay seen for Si in Fig.6.3 is expected to be mostly due to the fanning effect. Fig.6.4 shows the ratio between LiF data and Si fit. If there was no specular reflection increase due to closing of 2nd order diffraction, the ratio between LiF data and Si fit should be constant and close to one.

The second order diffraction peak corresponds to a wave vector of $k = 3.12\ 1/\text{Å}$ equal to a velocity of $v = 496.0\ m/s$. Thus, every incident particle with a velocity higher than v can undergo 2nd order diffraction. Taking the incident beam velocity of $v = (503 \pm 10) m/s$ (Eq.6.2), the second order will be closed above $f_{2nd} = (2.2 \pm 3.2) Hz$ spinning frequency. The higher the spinning frequency, the more atoms of the incident beam distribution cannot diffract to 2nd order. Thus, the specular reflection maximum is expected to lie above f_{2nd}.

As seen in Fig.6.4 there is a big discrepancy between the measured maximum in intensity and the calculated frequency f_{2nd}. Further experiments will have to show whether or not the measured maximum corresponds to f_{2nd}.

Yet, there are too many uncertainties in the measurement, since parameters, such as exact timing have to be optimized with further runs and the fanning effect has to be considered more carefully. Therefore, the effect of closing of $2nd$ order diffraction is still speculative. At the moment no conclusions can be drawn about the closing of diffraction channels.

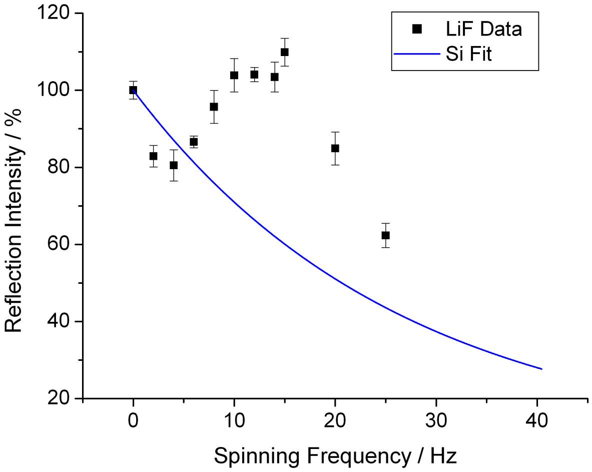

Figure 6.3: Detected reflection intensity at different rotor frequencies for LiF compared to Si data fitted by an exponential decay. Data is taken from previous experiments [7], normalized to the reflectivity at 0Hz (standing mirror) and given in percent.

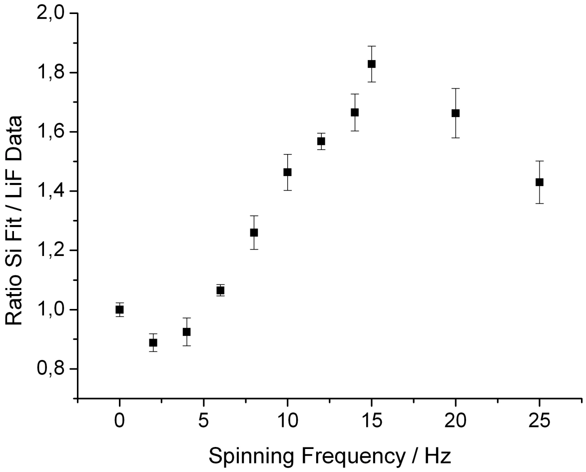

Figure 6.4: Ratio between LiF and the Si fit in Fig.6.3

Chapter 7

Conclusion and Future Work

Various improvements have been made on the rotor experiment. The rotor now can spin at higher frequencies, enabling further slowing of atomic beams. The chamber can be pumped down faster and kept at lower pressure due to the cryo-trap, which improves the crystal life time.

The process of producing atomically flat silicon (111) was tailored towards better surface quality, but it is not an optimal choice in terms of preparation and crystal life time. Especially the low reproducability makes it necessary to find a better material.

Our attention was brought to lithium fluoride often used for atom-surface diffraction experiments. Its capability for this experiment was tested and the setup has been adopted to the new mirror material. Various crystals with different purities or grown by different methods where tested. It turns out, radiation hardened LiF exhibits the best surface quality. Pure LiF is hardly cleavable due to its plasticity while radiated LiF results in a high defect density making the material more brittle. This material has a short preparation time of about 5 min compared to a few hours for silicon. It is easy to handle and prepare by cleaving. The crystal has a much longer life time due to its surface inertness.

We obtained first results as a proof of principle by reflecting ground state helium at up to 25Hz spinning frequency.

It turns out that we are restricted to low mass atoms. Higher masses result in an increase in the Debye-Waller factor leading to a decrease in the elastic scattering amplitude. Deuterium, D_2, although it has the same mass as helium, shows little reflectivity probably due to rotational inelastic diffraction and we were not able to observe a strong reflection signal. Molecular hydrogen, H_2, might be a candidate for this experiment, although the current detectors are not capable of detecting such low masses.

An interesting effect, motivating further studies, might be the possibility of closing 2nd order diffraction resulting in an increase in reflection intensity. Right now, more careful measurements have to be done to examine this possibility.

Cleaving is a quite general method of obtaining atomically flat surfaces. Alkali-, earth alkali-halides or other crystals, due to their similar cleaving characteristics, could easily be prepared and tested with the current setup. $NaCl$ or MgF_2 might be worth another try because of their good inertness but higher mass compared to LiF.

Big potential for improvement probably lies in the cleaving process. The crystal should be hardened towards higher brittleness. Magnesium doped LiF becomes more brittle with increasing concentration. F-centers are a promising method since the crystals used for this experiment are hardened by γ-radiation causing those centers. There should be an optimum in radiation dose as well as dopant concentration. An easy way of creating F-centers might be heating a crystal in steam of its metal [44], which is a known and documented process. The F-center concentration can be measured by the crystal color.

The cleaving apparatus has been designed to be extendable. A device for setting the force acting on the knife could be added on top of the device where a mass is dropping from a certain height on the knife extension.

By gaining further control over the cleaving process, in particular the crack velocity, one might be able to increase surface quality as well. There is a specific minimum time, an 'incubation time', to nucleate a dislocation. If the crack is faster than this critical velocity v_c, no dislocations are nucleated [31] [45]. This time window corresponds to the process of building up tension to cause slipping and to create a dislocation. Above the critical velocity v_c dislocation motion is also constrained. In brief, depending on the crack velocity the shape of the plastic zone as well as the tension (in means of strength and direction) on dislocations changes. This results in a force counter acting against the stress field in front of the crack tip impeding dislocation motion [20]. In theory, a crack advancing above the critical velocity would leave a perfectly flat surface behind. If one could control the crack velocity, one could obtain a very flat surface. One approach might be the following: the crack velocity does depend on the knife shape. While the crack advances, the knife penetrates further into the crystal. Depending on the knife shape the two new pieces will be pulled apart with a certain force. This force results in a strain field with it's maximum in front of the crack (those relations are known and can be calculated by classic beam theory and theory of elasticity). By carefully choosing a specially shaped knife one could obtain control of the crack velocity in terms of crack length and knife penetration depth.

Bibliography

[1] Harold J. Metcalf and Peter van der Straten. *Laser Cooling and Trapping.* Springer- Verlag, 1999.

[2] O. Carnal, M. Sigel, T. Sleator, H. Takuma, and J. Mlynek. Imaging and focusing of atoms by a fresnel zone plate. *Phys. Rev. Lett.*, 67(23):3231–3234, Dec 1991.

[3] R. B. Doak, R. E. Grisenti, S. Rehbein, G. Schmahl, J. P. Toennies, and Ch. Wöll. Towards realization of an atomic de broglie microscope: Helium atom focusing using fresnel zone plates. *Phys. Rev. Lett.*, 83(21):4229–4232, Nov 1999.

[4] Paul R. Berman. Atom interferometry. *Physics Today*, 1997.

[5] D.A. MacLaren and W. Allison. Microscopy with atomic beams: Contrast in a scanning helium microscope. *Inst. Phys. Conf. Ser. 179(10),(2004), 383-388*, 179:383–388, 2004.

[6] E. Narevicius, A. Libson, C. Parthey, I. Chavez, J. Narevicius, U. Even, and M.G. Raizen. Stopping supersonic oxygen with a series of pulsed electromagnetic coils: a molecular coilgun. *Phys. Rev. A 77,*, 77:051401 (2008)., 2008.

[7] E. Narevicius, A. Libson, M.F. Riedel, C.G. Parthey, I. Chavez, U. Even, and M.G. Raizen. Coherent slowing of a supersonic beam with an atomic paddle . *Phys. Rev. Lett.*, 98, 103201, 2007.

[8] Max Fabian Riedel. Elastic slowing of supersonic beams. Master's thesis, The University of Texas at Austin, 2006.

[9] H. Pauly. *Atom, Molecule, and Cluster Beams I.* Springer- Verlag, 2000.

[10] Yasin Ekinci. *High Resolution Scattering of He Atoms and D2 Molecules from the LiF(001) Crystal Surface.* PhD thesis, Georg-August-Universitat zu Goettingen, 2003.

[11] D.A. MacLaren. *Development of a Single Crystal Mirror for Scanning Helium Microscopy.* PhD thesis, University of Cambridge, March 2002.

[12] D.A. MacLaren, N.J. Curson, P. Atkinson, and W. Allison. An afm study of the processing of hydrogen passivated silicon(111) of a low miscut angle. *Surf. Sci.*, 490:285–295, 2001.

[13] J. Flidr, Y. Huang, T.A. Newton, and M.A. Hines. Extracting site-specific reaction rates from steady state surface morphologies: Kinetic monte carlo simulations of aqueous s(111) etching. *J. of Chem. Phys.*, 108,13:5542–5553, 1998.

[14] J. Viernow, J.-L. Lin, D. Y. Petrovykh, F. M. Leibsle, F. K. Men, and F. J. Himpseld. Regular step arrays on silicon. *Apl. Phys. Let.*, 72,8:948–950, 1998.

[15] K. A. Reinhard and Werner W. Kern. *Handbook of Silicon Wafer Cleaning Technology - 2nd ed.* William Andrew Inc., 2007.

[16] L. Estermann and O. Stern. Beugung von molekularstrahlen. *Zeitschrift für Physik A*, 61:95–125, 1929.

[17] Yu. Ya. Meshkov. Griffith energy criterion in the fracture micro-and macromechanics of brittle bodies. *Metal Science and Heat Treatment*, Volume 38:28–32, 1996.

[18] A. Griffith. The theory of rupture. In *Proc. 1st Int. Cong. for Applied Mechanics, Vol. 8, 5158.*, 1924.

[19] Alan T. Zehnder. *Lecture Notes on Fracture Mechanics.* Alan T. Zehnder, 2007.

[20] S. J. Burns and W. W. Webb. Fracture surface energies and dislocation processes during dynamical cleavage of lif. part 1: Theory. *J. of Appl. Phys.*, 41, 5:2078–2085, 1970.

[21] M. Marder and Jay Fineberg. Cracks cleave crystals. *Europhys. Lett.*, 66 (3):364–370, 2004.

[22] M. Marder. Molecular dynamics of cracks. *Computing in Science and Engineering*, 1:48–55, 1999.

[23] M. Marder and J. Fineberg. How things break. *Physics Today*, pages 24–29, 1996.

[24] Korth Kristalle GmbH. Lithium fluoride datasheet, Nov. 2008.

[25] RedOptronics. Lithium fluoride datasheet, Nov. 2008.

[26] H. Hoinkes, H. Nahr, and H. Wilsch. Surface debye temperature by atomic beam scattering. *Surface Science*, 33, Iss. 3:516–524, 1972.

[27] J. R. Bledsoe and S. Fisher. *Surf. Sci*, 46:1229, 1974.

[28] Alkor Crystal Optics. Material datasheet, Nov. 2008.

[29] J. Estel, H. Hoinkes, H. Kaarmann, H. Nahr, and H. Wilsch. On the problem of water adsorption on alkali halide cleavage planes, investigated by secondary ion mass spectroscopy. *Surface Science*, 54:393–418, 1976.

[30] J.L. Robins, T.N. Rhodin, and R.L. Gerlach. Dislocation structures in cleaved magnesium oxide. *J. of Appl. Phys.*, 37, Nr.10:3893–3903, 1966.

[31] J. J. Gilman, C. Knudsen, and W. P. Walsh. Cleavage cracks and dislocations in lif crystals. *J. of Appl. Phys.*, 29, No.4:601–607, 1958.

[32] F.C. Hallberg, B.E. Woodgate, and J.S.J. Benedicto. Cleaving machines for soft and hard crystals. *Rev. Sci. Instrum.*, 52(5):759– 762, 1981.

[33] M. Schmid, A. Renner, and F. J. Giessibl. Device for in situ cleaving of hard crystals. *Rev. of Sci. Instr.*, 77, 036101, 2006.

[34] Clemens Barth, Christian Claeys, and Claude R. Henry. Surface preparation of hard ionic crystals by ultrahigh vacuum cleavage. *Review of Sci. Instr.*, 76:083907, 2005.

[35] Superconix inc. 2440 Lisbon Avenue Lake Elmo, Minnesota 55042.

[36] MaTecK GmbH. Adr.: Im Langenbroich 20 - D-52428 Juelich.

[37] Rexon components inc. 24500 High Point Road, Beachwood, OH.

[38] Argus international ltd. 108 Whispering Pines Drive, STE 110, Scotts Valley, CA 95066.

[39] J.S. Nadeau and W.G. Johnston. Hardening of lithium fluoride crystals by irradiation. *J. Appl. Phys.*, 32:2563–2565, 1961.

[40] W.G. Johnston. Effects of impurities on the flow stress of lif crystals. *J. of Appl. Phys.*, 33:2050–2058, 1962.

[41] J. Borc and K. Sangwal. On the prefection of cleavage planes of potassium bichromate single crystals. *Surf. Sci.*, 601:1160–1166, 2007.

[42] G. Boato, P. Cantini, and L. Mattera. A study of the (100) lif surface at 80k by means of diffractive scattering of he and ne atoms at thermal energies. *Surf. Sci.*, 55:141–178, 1976.

[43] Y. Ekinci and J.P. Toennies. Thermal expansion of the lif(0 0 1) surface. *Surface Science*, 563:127134, 2004.

[44] G. Miessner. Farbzentren in alkalihalogenid-mischkristallen. *Zeitschrift fuer Physik A Hadrons and Nuclei*, 134(5):576–581, 1953.

[45] S. J. Burns and W. W. Webb. Fracture surface energies and dislocation processes during dynamical cleavage of lif. part 2: Experiments. *J. of Appl. Phys.*, 41:20862095, 1970.

[46] A. Ashkin. Atomic-beam deflection by resonance-radiation pressure. *Phys. Rev. Lett.*, 25(19):1321–1324, Nov 1970.

[47] D. Barredo. Si(111)h(1x1): A mirror for atoms characterized by afm, stm, he and h2 diffraction. *Surface Science*, 601:24–29, 2007.

[48] J. Borc and K. Sangwal. Study of elementary steps on the (001), (100) and (010) cleavage faces of potassium bichromate single crystals. *Surface Science*, 602:11751184, 2008.

[49] W. Demtroeder. *Experimentalphysik 3.* Springer- Verlag, 2005.

[50] Daniel Farias and Karl-Heinz Rieder. Atomic beam diffraction from solid surfaces. *Rep. Prog. Phys.*, 61:1575–1664, 1998.

[51] L.D. Landau and E.M. Lifshitz. *Theory of Elasticity.* Reed Educational and Professional Publshing Ltd., First published in english in 1959.

[52] J. Y. Lee and K.N. Subramanian. Fracture of lif bicrystals. *J. of Mat. Sci.*, 18:1765–1772, 1983.

Vita

Name:	Christoph Jan Schaeff
Date of Birth:	June 15th 1984
Place of Birth:	Erlangen, Germany

Education

09/1989	Elementary school, East Fishkill, NY, USA
10/1990	Elementary school in Daetzingen, Germany
09/1995	Elementary school in Lucas-Lossius Schule Reinhardshagen, Germany
09/1997	Grammarschool at the Grotefend-Gymnasium Hann.Muenden Germany
06/2004	Abitur at Grotefend-Gymnasium, Hann.Muenden, Germany
10/2004	Beginn of Physics Study at the Julius-Maximilians-Universitaet Wuerzburg, Germany Minor fields of study: Chemisty, Business Studies
10/2006	Vordiplom in Physics (Acknowledged as bachelor degree)
12/2008	Master of Arts in Physics at the University of Texas at Austin

Awards

2001	Second place in National German Physics Contest
09/2007-05/2008	Scholarship from DAAD (Deutscher Akademischer Austausch Dienst)

Permanent address: Leipziger Strasse 13, 34359 Reinhardshagen,
Germany

This thesis was typeset with LaTeX[†] by the author.

[†] LaTeX is a document preparation system developed by Leslie Lamport as a special version of Donald Knuth's TeX Program.